Leaky faults modulated magma ascent and seismicity during the 2022 São Jorge (Azores) volcanic unrest

Stephen P. Hicks[1,*,✢], Pablo J. Gonzalez[2,✢], Anthony Lomax[3], Ana M.G. Ferreira[1], Ricardo S. Ramalho[4], Neil C. Mitchell[5], Graça Silveira[6,7], Nuno Afonso Dias[6,7], João Fontiela[8], Rui Fernandes[9,6], Susana Custódio[6], Maria Tsekhmistrenko[1], Virgilio Mendes[6], Adriano Pimentel[10,11], Rita Silva[10,11], Gonçalo Prates[12,13], William Sturgeon[1], Augustin Marignier[1], Fernando Carrilho[14], Rui Marques[10,11], Miguel Miranda[6,15], Arturo M. Garcia[10,11].

1. Department of Earth Science, University College London, London, United Kingdom.
2. Volcanology Research Group, Department of Life and Earth Sciences, Instituto de Productos Naturales y Agrobiología, Consejo Superior de Investigaciones Científicas (IPNA-CSIC), La Laguna, Spain.
3. ALomax Scientific, Mouans Sartoux, France.
4. School of Earth and Environmental Sciences, Cardiff University, Cardiff, United Kingdom.
5. Department of Earth and Environmental Sciences, University of Manchester, Manchester, United Kingdom.
6. Instituto Dom Luiz, Faculdade de Ciências, Universidade de Lisboa, Lisbon, Portugal.
7. Instituto Superior de Engenharia de Lisboa, Instituto Politécnico de Lisboa, Lisbon, Portugal
8. Institute of Earth Sciences, University of Évora, Portugal.
9. University of Beira Interior, Covilha, Portugal.
10. Instituto de Investigação em Vulcanologia e Avaliação de Riscos (IVAR), Universidade dos Açores, Azores, Portugal.
11. Centro de Informação e Vigilância Sismovulcânica dos Açores (CIVISA), Azores, Portugal.
12. Instituto Superior de Engenharia, University of Algarve, Faro, Portugal.
13. Centro de Estudos Geográficos, IGOT, University of Lisbon, Lisbon, Portugal.
14. Divisão de Geofísica, Instituto Português do Mar e da Atmosfera, Lisbon, Portugal.
15. AIR Centre, Azores, Portugal

* Corresponding author (email: stephen.hicks@ucl.ac.uk)

✢ Equally-contributing authors

Abstract

Understanding the signatures and mechanisms of failed volcanic eruptions is vital for mapping magma plumbing systems and forecasting volcanic hazards. Geological structures like fractures and faults are key to guiding magma, but their mechanisms remain unclear due to limited 3-D mapping of faults in volcanic regions and sufficiently precise earthquake locations. The triple-junction setting of the Azores Archipelago, where volcanic systems and seismogenic crustal faults coexist, offers a unique window into how faults impact magmatism. Using ~12,000 earthquakes relocated to ultra-high precision with onshore and ocean-bottom seismometer data, along with geodetic observations and seismic autocorrelation imaging, we analyse a failed eruption in 2022 on São Jorge Island. Magma from the upper mantle ascended rapidly and largely aseismically over several days along a crustal fault, before stalling beneath the island edifice. Adjacent seismicity with rotated focal mechanisms suggests that the ascending magma became less buoyant due to devolatilisation, with fluids leaking laterally along the fault zone, triggering an intense, months-long seismic swarm. This study reveals the dual role of fault zones in both facilitating and arresting magma ascent, highlighting the interplay between tectonism and magmatism.

1. Introduction

Magma that ascends to Earth's surface causes volcanic eruptions, but it can also stall at various depths, including the shallow crust, leading to *failed* eruptions[1]. Understanding the mechanisms of magmatic ascent is key to interpreting volcanic unrest and crust formation. The final fate of magma depends on several factors like its pressure relative to the crustal rock stress state[2] and internal magma dynamics (e.g., degassing, resupply of magma, devolatilisation[3], crystallisation[1]).

Pre-existing faults and fractures play a crucial but underexplored role in magma dynamics. Faults can capture and guide melt[4], providing energetically favourable pathways[5–7] for it to reach the surface[6,8]. Alternatively, stalling of magma may occur due to fluid circulation[9], or if the fault is misoriented for opening[8,10]. While fault architecture influences fluid flow and seismic activity[11], the mechanical link between faults and magmatism remains poorly understood[12–14]. Spatio-temporal patterns of volcano-tectonic (VT) seismicity can reveal magma pathways[15,16]. However, a key challenge in disentangling the role of faults and fractures is obtaining sufficiently accurate and precise earthquake locations relative to fault length-scales[17], particularly problematic in ocean island settings where seismograph coverage is limited by island and inter-island geography.

In contrast to classical orthogonal rifts (e.g., Afar, East Africa), transtensional environments provide insight into the interaction between pre-existing faulting structures and magmatism, and how they accommodate plate motion. In SW Iceland, dikes strike perpendicular to tectonic extension[6], triggering seismicity along oblique faults that accommodate the strike-slip component of plate motion[18]. Such cases somewhat conceal the more direct role of faults in magma ascent, leaving a gap in our understanding of how larger, proximal faults influence magma movement[19] and feedback mechanisms between tectonics, magmatism and seismogenesis.

Unlike Iceland, the coexistence of active magmatic systems and seismogenic crustal-scale faults in the Azores hotspot and triple-junction region offers a clear view of the interplay between tectonic structures and magmatism[20] (Fig. 1a). The Azores is shaped by the diffuse boundary between the Eurasian and Nubian plates, with the Terceira Rift (TR) (Fig. 1a) as the main spreading system, where slow (~4.5 mm/yr), WSW-ENE-oriented relative motion[21–24], produces right-lateral transtension[25]. Earthquakes[26–28] include rift-parallel normal faulting and off-rift strike-slip faulting (Fig. 1a). Deformation across the Azores is highly distributed, with fissure systems, off-rift transforms, grabens, and extension-oblique volcanic ridges[20,21,25,29–35], such as that expressed by São Jorge Island, located ~40 km SW of the TR (Fig. 1b).

São Jorge is a narrow island 55 km long and up to 7 km wide. Erupted basalts show signs of a weak mantle plume[36], with fissure eruptions generally migrating 5cm/yr westwards over 750 kyr[21]. These rifts lie along strike-slip fault zones, reflecting magmatic-tectonic interplay[21,23]. In the west, two major fault zones (Fig. 1c, Fig. 2), Picos (P-FZ; striking WNW–ESE) and Pico do Carvão (PdC-FZ; striking almost E-W) feature volcanic cones and craters[34]. The PdC-FZ hosted eruptions in 1580, and 1808, with a possible submarine eruption in 1964[23,37]. Historically, the island hosted one of the largest earthquakes in the Azores, an estimated *M* 7.5 in 1757[38–41]. Paleoseismology shows the right-laterally offset PdC-FZ (Fig. 2) is the fastest-slipping fault (2.6-3.4 cm/yr) on São Jorge[42] and can generate *M*~7 earthquakes[34,42].

In March 2022, São Jorge experienced a highly active seismic swarm[43,44], with microseismicity continuing for at least two years. Ultra-high-precision hypocentre locations from onshore and offshore seismic data, reconciled with ground deformation observations reveal a crustal fault acting as a pathway and a barrier to magma ascent.

2. Results

2.1. Geodetic observations and dike-opening model

Daily GNSS solutions from nine stations in the Azores (Fig. 1b; see *Methods*) show intense deformation beginning on 19 March 2022, when the seismic swarm commenced (Figs. 3a, S1-S2). Stations on Pico (PIED; AZTP) and Graciosa (AZGR; ENAO) moved horizontally away from São Jorge by up to 18 mm (Fig. 1b). Faial (HORT) and Terceira (PAGU; TERC) show negligible motion. São Jorge stations (QEMD, VLAZ) moved roughly eastward by up to 10 mm. QEMD shows rapid deformation over just one day, while AZTP shows a slightly slower, three-day-long deformation (Fig. S2). Aside from long-term interplate strain accumulation, no significant deformation occurred before or after the seismicity (Figs. 3a, S1 & S2).

Analysis of Sentinel-1A interferograms reveals no significant deformation signals before or after the seismicity onset (Fig. S3-S5; see *Methods*). During 15-21 March 2022, independent interferograms spanning 2022-02-13 to 2022-03-21 (ascending) (Figs. 1c & S4) and 2022-03-15 to 2022-03-27 (descending) detected up to +6 cm line-of-sight deformation on central São Jorge (Figs. 1c & S4). Both ascending and descending passes show a similar uplift pattern, symmetrical across the island's flanks, with maxima at the coastlines ('L1' and 'L2' in Fig. 1c) and negligible deformation along an 8-10 km saddle sub-parallel to the island's axis. All deformation detected by InSAR occurred between 15 and 21 March 2022 (Figs. S3-S5), consistent with the GNSS signals and seismicity onset.

InSAR fringe patterns and GNSS displacements north and south of São Jorge indicate a magma intrusion striking slightly oblique to the island's axis. Joint inversion of GNSS and InSAR data (see *Methods*) yield a model (Fig. 4; Table S1; Figs. S9-12) comprising a ~6 km-long, WNW-ESE (285° strike), near-vertical (83° dip) dike beneath the western-central island, east of the seismicity. The dike has a maximum opening of 72 cm, with its top at ~1.65 ± 0.60 km below the surface and bottom at ~26 ± 8 km below sea level, within the lithospheric mantle[45,46].

2.2. Seismicity distribution and its temporal evolution

Seismic data come from permanent networks densified by temporary stations installed in response to the seismic swarm (Fig. 1b); (see *Methods* & Data Availability). Six temporary ocean bottom seismometers (OBS) offshore São Jorge improve the inherently poor coverage due to the geographic distribution of the islands and the narrow geometry of São Jorge (Fig. 1b). Using data from 83 stations, our automated workflow (see *Methods*) gives ultra-high precision relative-relocations for 11,967 events, with a median depth uncertainty of 46 m.

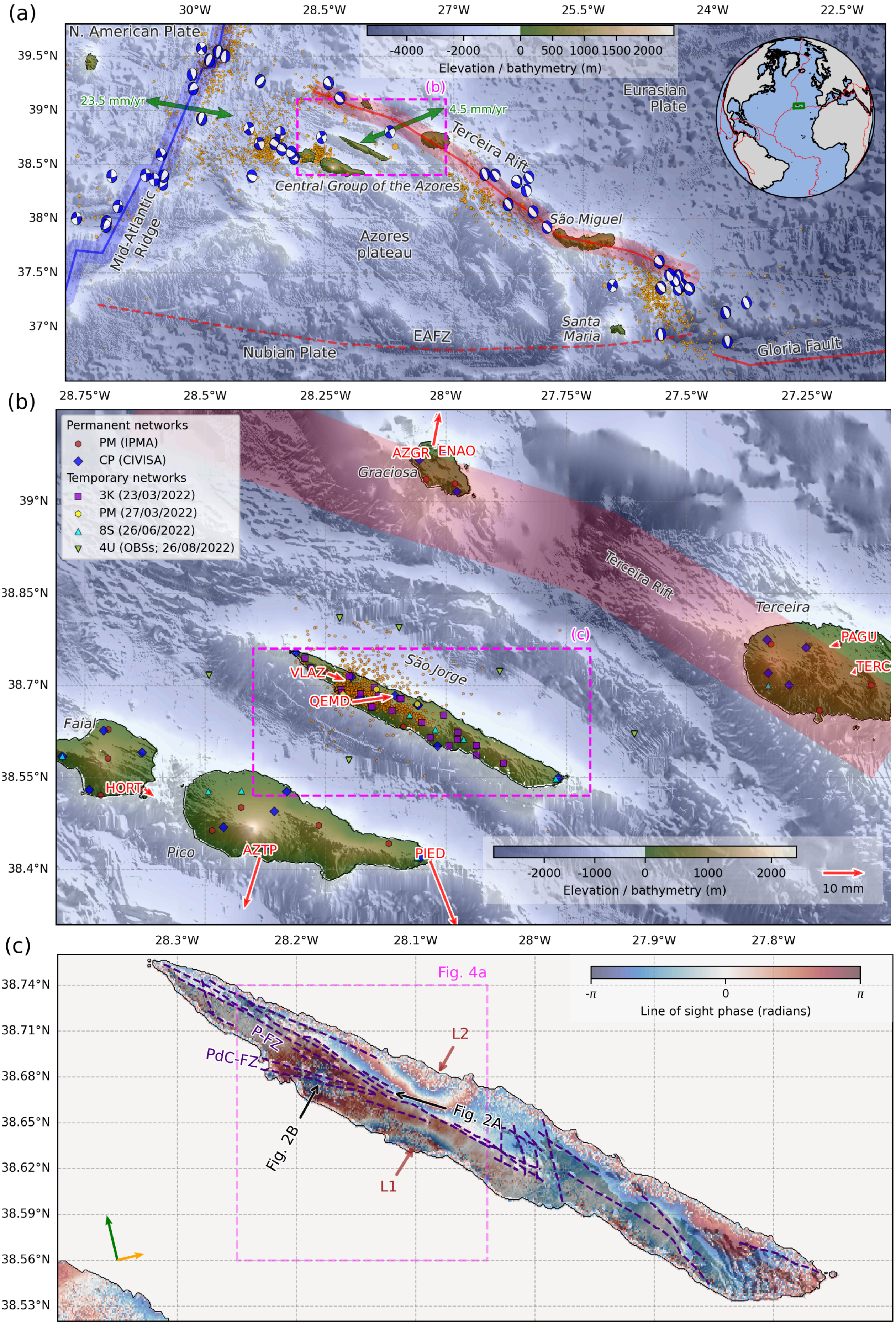
(a)
30°W
28.5°W
27°W
25.5°W
24°W
22.5°W
39.5°N
39°N
38.5°N
38°N
37.5°N
37°N
N. American Plate
-4000
-2000
0
500
1000
1500
2000
Elevation / bathymetry (m)
(b)
23.5 mm/yr
4.5 mm/yr
Eurasian Plate
Terceira Rift
Central Group of the Azores
São Miguel
Mid-Atlantic Ridge
Azores plateau
Santa Maria
EAFZ
Nubian Plate
Gloria Fault
(b)
28.75°W
28.5°W
28.25°W
28°W
27.75°W
27.5°W
27.25°W
39°N
38.85°N
38.7°N
38.55°N
38.4°N
Permanent networks
PM (IPMA)
CP (CIVISA)
Temporary networks
3K (23/03/2022)
PM (27/03/2022)
8S (26/06/2022)
4U (OBSs; 26/08/2022)
AZGR
ENAO
Graciosa
Terceira Rift
Terceira
PAGU
TERC
(c)
São Jorge
VLAZ
QEMD
Faial
HORT
Pico
AZTP
PIED
-2000
-1000
0
1000
2000
Elevation / bathymetry (m)
10 mm
(c)
28.3°W
28.2°W
28.1°W
28°W
27.9°W
27.8°W
38.74°N
38.71°N
38.68°N
38.65°N
38.62°N
38.59°N
38.56°N
38.53°N
Fig. 4a
-π
0
π
Line of sight phase (radians)
L2
P-FZ
PdC-FZ
Fig. 2A
Fig. 2B
L1

Fig. 1: Seismotectonic context, stations, and surface deformation. *a) Tectonic configuration of the Azores region, showing pre-2022 M>3.5 background seismicity (orange circles)*[47]*. Double-couple components are plotted for moment tensors*[27]*. Green arrows show relative plate motions*[22]*. EAFZ = East Azores Fracture Zone. b) Map of the Central Group islands of the Azores showing locations of permanent and temporary seismic stations. Red arrows show horizontal GNSS solution displacement vectors from 17/03/2022 - 22/03/2022, with station names labelled in red. Orange circles show the routine seismic locations of the 2022 seismic swarm from CIVISA. c) Wrapped ascending interferogram from the Sentinel-1A satellite spanning 2022/02/13 - 2022/03/21. Green and orange arrows show the satellite azimuth and look direction, respectively. The brown annotations show the two lobes of uplift in the interferogram. Dark blue dashed lines show mapped faults and volcanic alignments on São Jorge*[34,42]*. Black arrows show the aerial imagery in Fig. 2.*

Precursory seismicity

We find deep clusters of M_L 1.0-2.5 events at ~30 km depth bsl south of São Jorge (Fig. 4a), starting seven months before the unrest. Our high-precision relative relocations show that these events, forming three main clusters, progressively migrated northward (labelled Deep, *DP1*-3 in Figs 4a-b), starting beneath the Canal de São Jorge (São Jorge channel, south of São Jorge Island), to ~2 km inland of the coastline, gradually shallowing from ~32 km to ~25 km depth (Fig. 4b). Waveform template matching[48] with these well-located events yields ~150 similar earthquakes (Fig. 3c) showing discontinuous, short bursts of seismicity during this migration, separated by longer aseismic periods. The seven weeks immediately before the onset of the seismic swarm was aseismic.

Seismic swarm

The seismic swarm that started abruptly on 19 March 2022 has an overall *b*-value, based on M_w estimates from spectral inversion (see *Methods*), that is remarkably high (2.4±0.1) (Fig. S7), with M_w 2.4 completeness, likely due to the evolving seismic station coverage. Seismicity appears as high-frequency signals with impulsive onsets, typical of VT events, with no evidence of long-period events or volcanic tremor.

Epicentres form a narrow (<500 m width), WNW-ESE lineation along the mapped surface trace of the PdC-FZ (Fig 4a), slightly oblique to the island's long axis. All events after 19 March 2022 lie between 6-14 km depth, most concentrated at 9-12 km (Fig. 4). In a cross-section perpendicular to the PdC-FZ (Fig. 4c), events at 9-12 km form a near-vertical structure dipping NNE with distinct sub-streaks. On a PdC-FZ-parallel cross-section (Fig. 4d), most events align along two gentle (~10°) west-dipping lineations: one at 9-11 km depth (labelled Upper Lineation, “UL” in Fig. 4d) with substantial internal complexity showing many sub-vertical streaks (Fig. 5) and the other at 11-12 km with sub-horizontal streaks (Lower Lineation, “LL” in Fig. 4d). These are separated by a ~2 km-wide aseismic region (“AS” in Fig. 4d). Additional seismic clusters and streaks occur below, at 12-14 km, with two diffuse zones of sparser seismicity extending upwards to ~6 km depth from the eastern edges of UL and LL (labelled Shallow, “SH” in Fig. 4c-d).

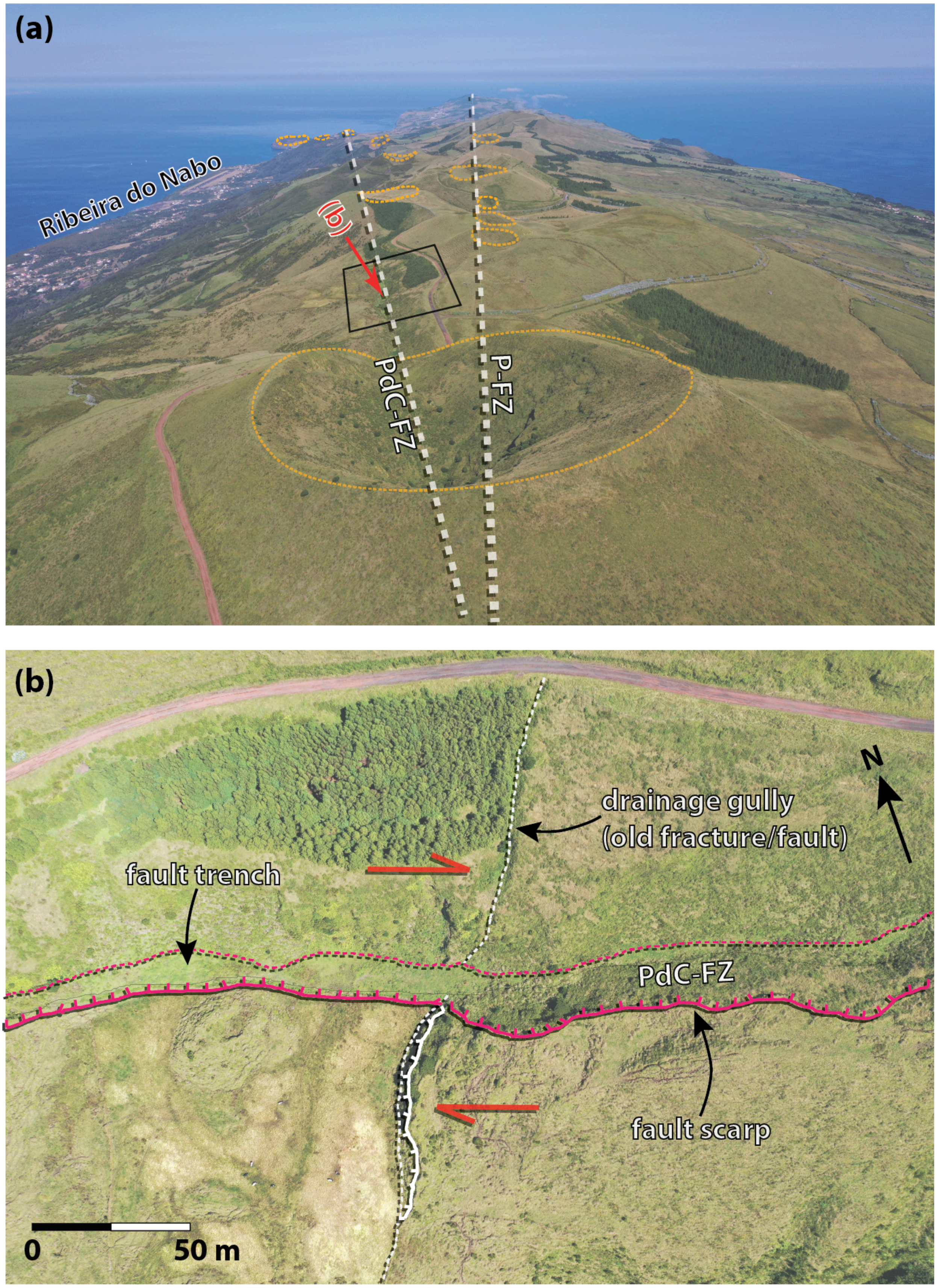

Fig. 2: Drone imagery showing surface faulting on São Jorge near the 2022 unrest. *P-FZ = Picos fault zone; PdC-FZ = Pico do Carvão fault zone. (a) View looking west-north-west (see Fig. 1c for camera position and direction). Dotted orange lines highlight ancient fissure eruption cones. (b) Evidence of right-lateral offsets along the PdC-FZ (see Fig. 1c and Fig. 3a for location).*

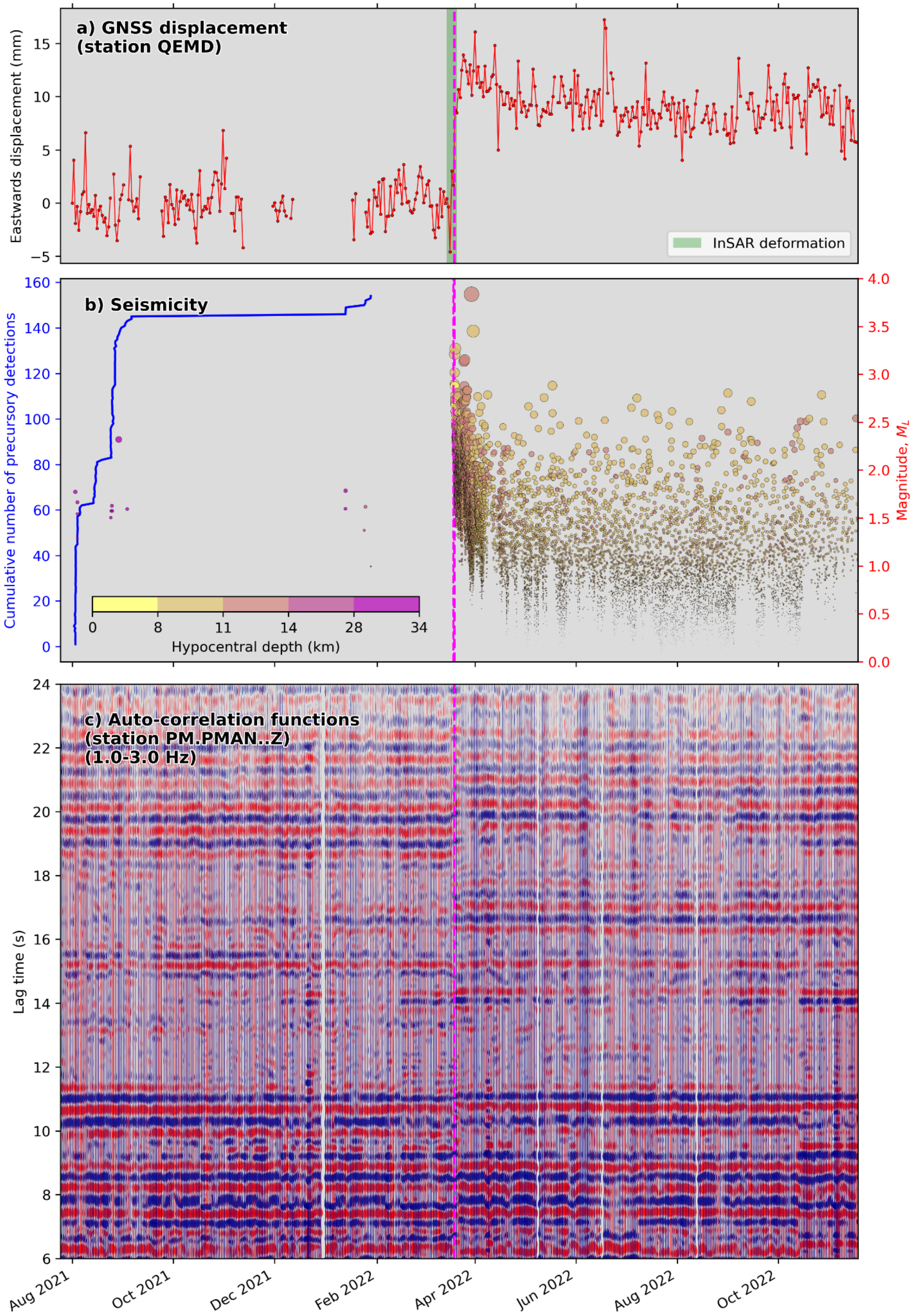
a) GNSS displacement
(station QEMD)
Eastwards displacement (mm)
15
10
5
0
−5
InSAR deformation
b) Seismicity
Cumulative number of precursory detections
160
140
120
100
80
60
40
20
0
0
8
11
14
28
34
Hypocentral depth (km)
Magnitude, M_L
4.0
3.5
3.0
2.5
2.0
1.5
1.0
0.5
0.0
c) Auto-correlation functions
(station PM.PMAN..Z)
(1.0-3.0 Hz)
Lag time (s)
24
22
20
18
16
14
12
10
8
6
Aug 2021
Oct 2021
Dec 2021
Feb 2022
Apr 2022
Jun 2022
Aug 2022
Oct 2022

Fig. 3: Evolution of the 2022 São Jorge unrest and precursory seismicity. *The vertical magenta dashed lines show the onset of the seismic swarm on 19 March 2022. a) Processed daily eastwards GNSS displacements at station QEMD (location shown in Fig. 1b), with the inferred period of InSAR detectable deformation labelled (Figs. 1c, S3 & S4). Displacements are given within a global reference frame, with the secular trend removed. Time series for other GNSS stations are shown in Figs. S1-S2. b) Time evolution of seismicity from our refined catalogue and matched-filter detections of deep (~30 km) precursory events. c) Autocorrelation results from the vertical component of station PM.PMAN (Fig. 4a) show changes in subsurface properties at the onset of the seismic swarm.*

Seismicity shows clear spatial migration over time (Fig. 4c-d; Movie S1). The first event in our catalogue (~1700 UTC, 19 March 2022) occurred in the shallow ("SH") zone of seismicity (~6 km depth). Within hours, activity shifted westward and downward into zones LL and UL. Initially, LL was most active, but UL became dominant after ~1 week, and by ~4 weeks, all events were confined to UL. We find highly similar waveforms for many events, yielding distinct families of events (Fig. 5).

Well-constrained focal mechanisms (see *Methods*; Fig. S8) show strike-slip faulting, with one nodal plane parallel to the main lineation of seismicity and the PdC-FZ, indicating left-lateral faulting. Dense coverage of the focal sphere indicates double-couple failure (Fig. S6).

2.3. Subsurface velocity changes

To study subsurface structural changes before, during, and after the seismic swarm, we analysed ambient noise phase autocorrelation functions[49] (ACF) at two permanent stations on São Jorge, PM.PMAN and PM.ROSA (Fig. 4a), yielding the underlying *P*-wave reflection response (see *Methods*). Pre-unrest reference ACFs from May to September 2021 show coherent arrivals at lag times of ~2-24 s. When the swarm began on 19 March 2022, PM.PMAN's ACFs showed a sharper shift to higher lags, especially in the 6-11 s and 18-23 s ranges, indicating velocity reductions at <10 km and >15 km depth, respectively, based on our 1-D velocity model (Fig. S6). Stronger reflections also appear at 16-18 s. PM.ROSA's ACF shows much fewer variations (Fig. S13).

3. Discussion

Using our high-precision seismicity catalogue, focal mechanisms, geodetic model, and seismic autocorrelation imaging, we have developed a model for the 2022 São Jorge seismic-volcanic unrest, illustrated in Fig. 6a and detailed below.

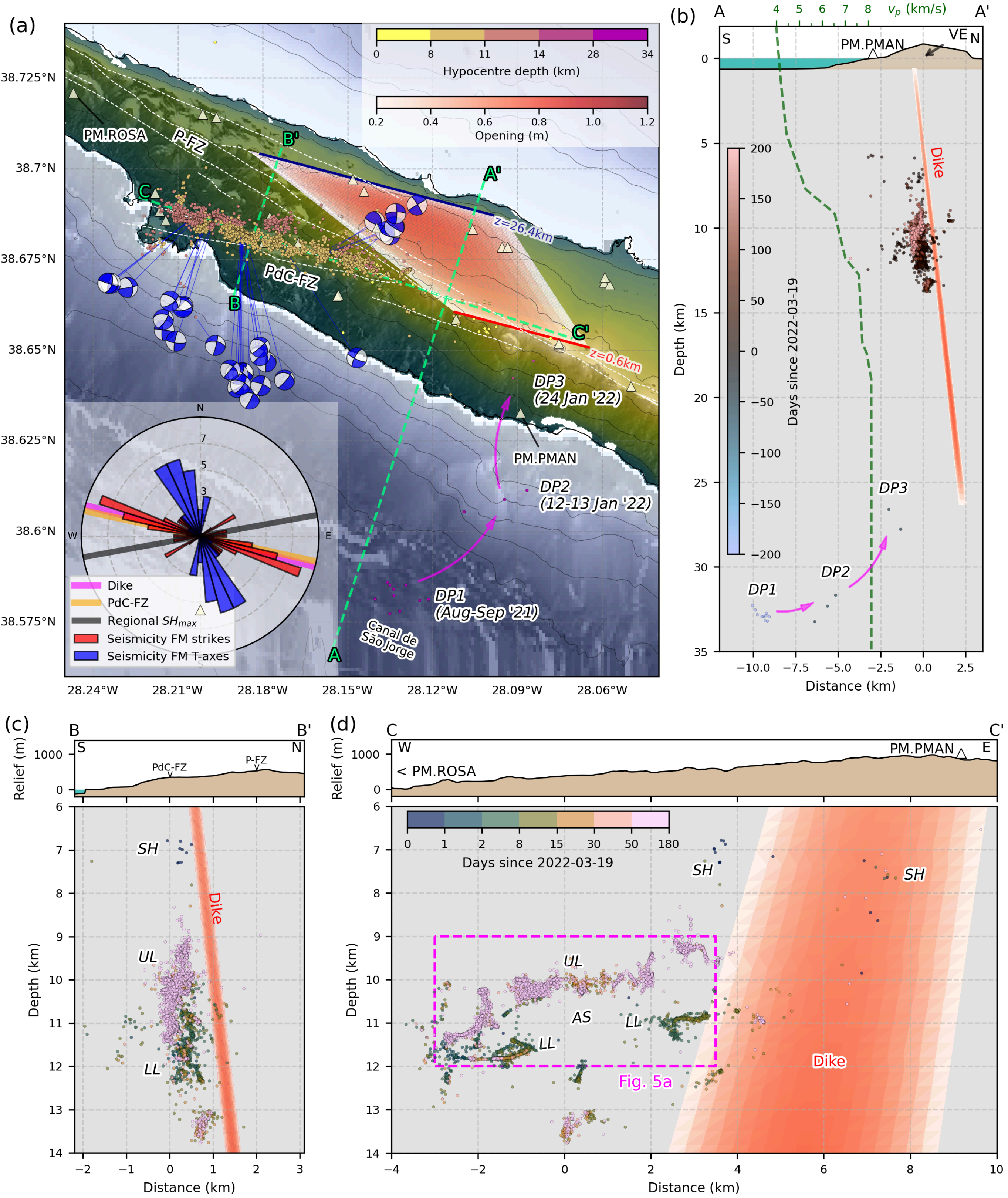

Fig. 4: High-precision seismicity relocations and joint GNSS-InSAR dike opening model. *(a) Map view, with seismic events coloured according to their depth. White dashed lines are surface fault traces and volcanic alignments*[23,42]*. Purple arrows show the migration of precursory seismicity. White triangles are seismic stations. Contour lines are plotted for every 250 m of elevation. The inset rose diagram shows focal mechanism strikes compared with the dike and mean strike of mapped faults, along with a comparison between the inferred regional SHmax direction (Fig. 1a) and focal-mechanism T-axes. (b) Seismicity-perpendicular cross-section, A-A'. VE = volcanic edifice. The dashed green line shows the P-wave velocity from our 1-D model (Fig. S6). c) Seismicity-parallel cross-section, with a focus on the main clusters of seismicity. d) Along-strike cross-section, C-C'. Labelled clusters of seismicity are discussed in the text. Note the break in range of the vertical axes between the relief and seismicity cross sections in (c) and (d).*

Our geodetic dike opening model indicates magma intrusion from 1-26 km depth bsl (Fig. 4), with no significant inflation preceding it (Figs. S1 & S3). The depth of precursory earthquakes in the upper mantle (25–35 km depth) correlates with the modelled dike's base (Figs. 3-4) and fluid inclusion barometry results from São Jorge lavas[50,51]. Such deep precursory seismicity[17,52–54] is often linked to magma accumulation or destabilisation in deep reservoirs[55–57]. Rapid geodetic deformation over a few days (Fig. 3a) suggests swift magma ascent with nearly simultaneous dike opening in the crust and upper mantle; this is supported by our ambient noise ACF results, showing rapid structural changes near the dike (Figs. 3d & 4). Such rapid magma ascent presents a challenge for tracking dike intrusions and forecasting the potential for their eruption, especially given that the ascent is almost exclusively aseismic, apart from a diffuse, shallow (~6 km depth) streak of seismicity during the first hours of the swarm, likely marking the edges of the ascending dike ('*SH*' in Fig. 4).

Our model shows that magma stalled ~1,600 m below the surface, near the estimated base of the island edifice, based on surrounding bathymetry. Compressive stress from the edifice load likely reduced the intrusion's buoyancy[58,59], while a dynamic rise in its viscosity[3] during ascent may have further promoted stalling.

The dike intruded parallel to the PdC-FZ and VT seismicity zone, east of the mapped fault zone where it is likely buried by lavas and scoria cones (Fig. 4). The fault therefore provides a direct structural connection between the dike and seismicity. Unlike typical dike intrusions, where seismicity surrounds the dike in a 'dogbone' pattern[15,60–67], the 2022 São Jorge event showed seismicity confined to one side, with no activity near or elsewhere around the dike, except for the shallow "*SH*" zone linked to dike ascent. The PdC-FZ and seismicity lie in a positively stressed zone (>50 kPa; Fig. S14), but similarly oriented nearby structures, like the P-FZ, remained aseismic. This suggests the PdC-FZ was more pre-stressed and closer to failure. The PdC-FZ is thus a major mantle-rooted structure in the central Azores that accommodates regional transtension[23,37,42,51], especially given its recent eruptive history and that it has generated Mw~7 earthquakes[42], likely involving full crustal rupture.

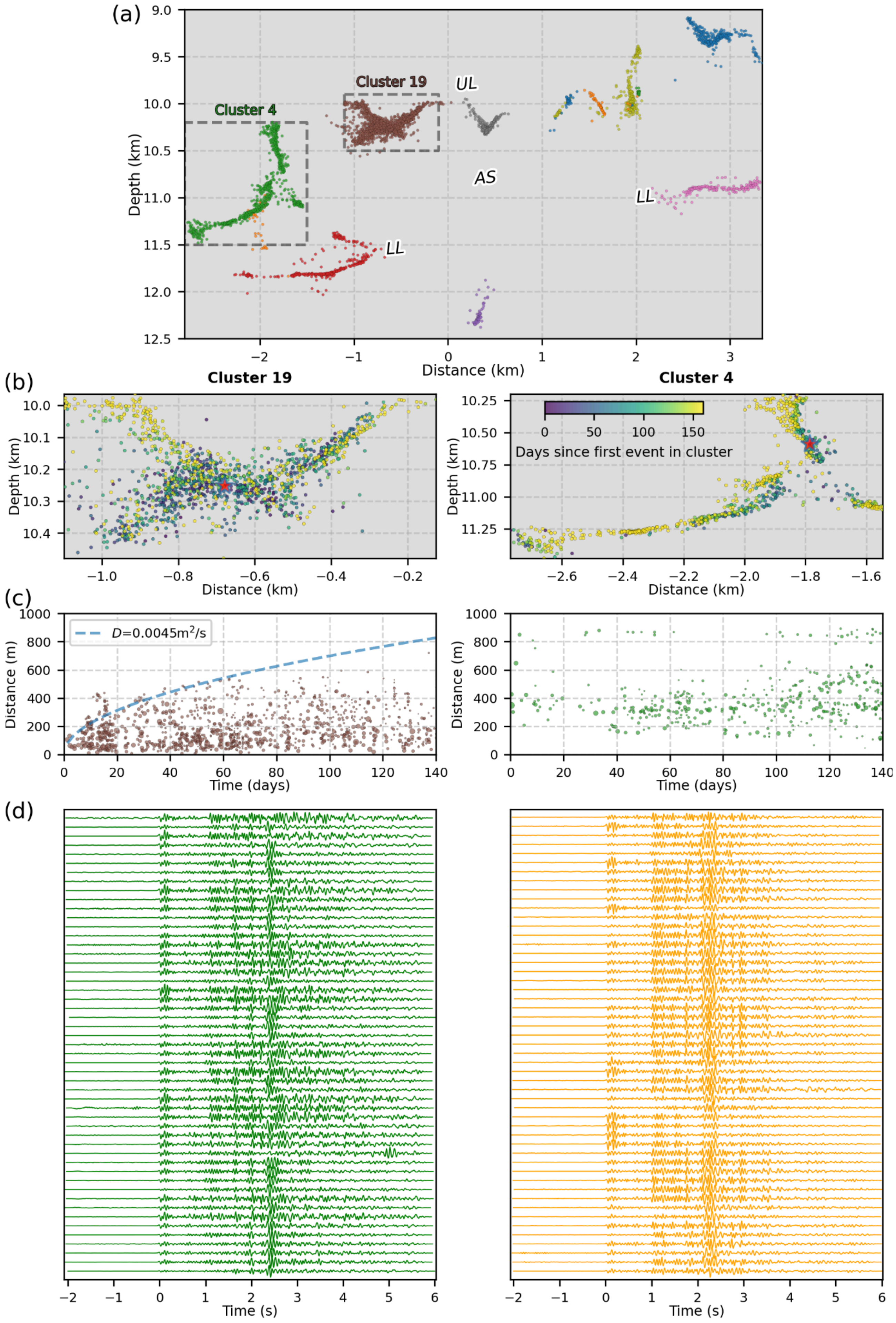
(a)
Cluster 19
Cluster 4
UL
AS
LL
LL
Depth (km)
9.0
9.5
10.0
10.5
11.0
11.5
12.0
12.5
−2
−1
0
1
2
3
Distance (km)
(b)
Cluster 19
Cluster 4
Depth (km)
10.0
10.1
10.2
10.3
10.4
−1.0
−0.8
−0.6
−0.4
−0.2
Distance (km)
10.25
10.50
10.75
11.00
11.25
−2.6
−2.4
−2.2
−2.0
−1.8
−1.6
0
50
100
150
Days since first event in cluster
(c)
D=0.0045m^2/s
Distance (m)
0
200
400
600
800
1000
0
20
40
60
80
100
120
140
Time (days)
(d)
−2
−1
0
1
2
3
4
5
6
Time (s)

***Fig. 5: Seismic event clustering**. (a) Zoomed-in view of the main zone of seismicity along the strike-parallel cross-section (Fig. 4d), with events coloured by their family based on waveform correlation clustering. The panels below show the details of two distinct clusters: 4 and 19. b) Zoomed-in view of these two seismicity clusters, with events coloured by their time relative to the first event in each cluster. c) Events in each cluster plotted as a function of time and distance relative to the first event in each cluster. For Cluster 19, the blue dashed line gives an approximate diffusivity effect fit to the migrating seismicity front. d) Examples of highly similar waveforms (P-wave cross-correlation coefficient >0.87 with the first earliest in each cluster) in the frequency band 2-40 Hz, with a maximum of 50 events shown for visualisation.*

The highly active swarm had an unusually high *b*-value of ~2.4, compared to the global volcanic average of ~1.7[68–70], likely due to the fluid-rich environment[71] along the PdC-FZ in the lower crust. The total seismic moment (~10^{16} Nm, or M_w 4.7) was large relative to the intrusion volume (~10^8 m^3) compared to other dike-related VT sequences[69,72] (Fig. 6b), slightly tending toward seismicity caused by fluid injection, which has greater seismic efficiency than most volcanic sequences[69] (Fig. 6b); thus indicating volatiles/fluids driving seismicity along the PdC-FZ. An important question is whether these were pre-existing hydrothermal fluids, or melt or volatiles were introduced by the intrusion. The ~2 km thick aseismic zone between two seismic lineations ('UL' and 'LL,' Fig. 4) may indicate a lateral magma branch[65,73,74]; however, forward modelling (see *Methods*) indicates that the geodetic observations do not support a substantially wide branch of magma filling the aseismic zone (Fig. S15). Some seismic clusters, such as Cluster 19 (Fig. 5; Movie S1), show complex fracture geometries and a migrating front with slow diffusivity (0.0045 m^2/s), suggesting upward fluid migration along propagating fractures[75] in the PdC-FZ.

Lacking evidence for magma directly triggering seismicity, we propose that fluid pore pressure increases, driven by thermal pressurisation[76] and magma devolatilisation[77–80], drove the seismicity. The PdC-FZ likely facilitated fluid channelling[81] through the lowermost crust near the crust-mantle boundary. Such fluids may come from regional mantle water enrichment[82]. Exsolution and subsequent devolatilisation, primarily of water, increased magma viscosity[3,58,83], causing the dike to stall ~1.6 km below the surface. This dynamic viscosity increase led to left-lateral shear failure along the PdC-FZ, contrasting with the background right-lateral motion[20,21,25,29–32,34,42] (Figs. 1a, 2, 4a), and induced a 90° focal mechanism rotation due to shear dilatancy effects counteracting the background stress[12,14,77,84,85].

Our findings highlight clear volcano-tectonic interactions that can be best observed transtensional environments. The dike intruded oblique to the minimum compressive stress (Fig. 4a), but was guided by the PdC-FZ, acting as a transtensional rift in the central Azores. The intrusion likely targeted a weaker fault segment near the PdC-FZ and P-FZ junction (Fig. 4a). The PdC-FZ, capable of generating *M*~7[25,34,42] earthquakes, likely exhibits along-strike variations in strength and coupling[86,87]. The seismic swarm, confined to the lowermost crust (Figs. 4 & 6a), possibly marks a rheological transition separating the locked shallow fault from the creeping upper mantle (Fig. 6). While the dike increased PdC-FZ stress for both left- and right-lateral slip modes (Fig. S14), the seismic swarm released only

M_w 4.7, leaving the likelihood of a future large earthquake uncertain. Such crustal faults in the Azores may result from repeated dike intrusions over time[30,88,89].

Our results suggest that pre-existing faults can have opposing effects on magma propagation. The PdC-FZ facilitated rapid vertical melt ascent, but may also have caused magma to stall by allowing lateral devolatilisation, increasing viscosity and pressure. The Azores thus offers new insights into the interplay between magmatism and seismic cycles.

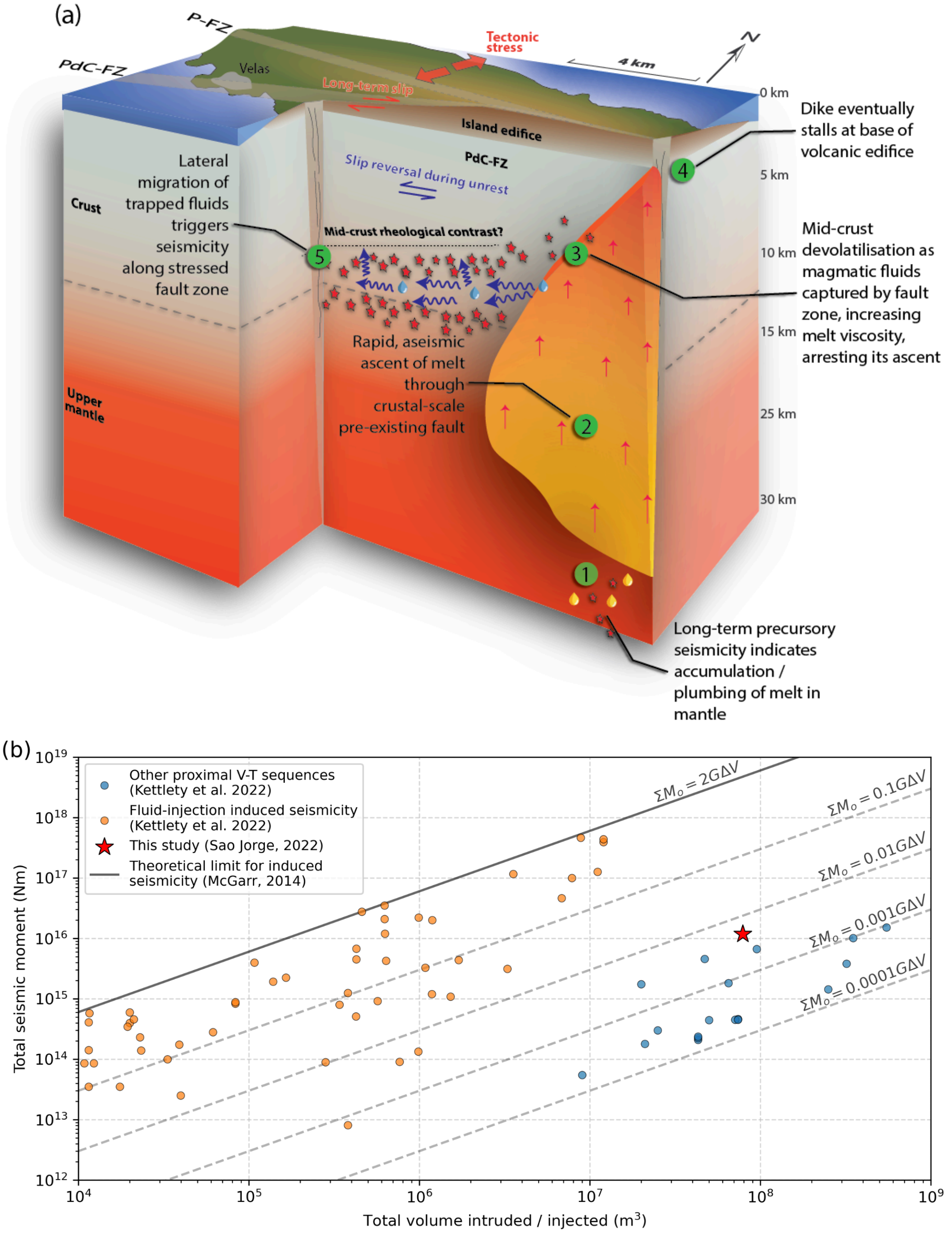

Fig. 6: Interpretation and global comparison. *a) 3-D schematic view cut along the strike of the PdC-FZ and the intruded dike showing the processes driving the São Jorge seismic-volcanic unrest in 2022. Note the exaggerated width of the dike. b) Comparison of intrusion volume versus total seismic moment with other proximal volcano-tectonic (V-T) sequences and fluid injection-induced seismicity[69]. Grey dashed lines show orders of magnitude smaller scaling to the McGarr[90] relationship to account for comparatively lower seismic efficiency in volcanic settings[69]. These relationships are shown with a shear modulus, G = 30 GPa.*

Methods

1. Satellite radar interferometry (InSAR) processing

InSAR displacement measurements are obtained by analysing phase differences between radar images acquired by the Sentinel-1A satellite, which are then utilised to generate displacement maps, also known as interferograms[91]. At São Jorge, we processed descending (track orbit number 082) and ascending (track orbit number 002) interferograms using the Hybrid Pluggable Processing Pipeline [92]. We analysed all Sentinel-1A data from 01 January 2022 to 31 July 2022, approximately three months before and after the onset of the unrest. Sentinel-1A images were processed at a multilook factor of 10 pixels in range and 2 pixels in azimuth, resulting in a pixel spacing of about 40 m. Topography phase contributions were removed using the COPERNICUS GLO-30 Global Digital Elevation Model (https://portal.opentopography.org/raster?opentopoID=OTSDEM.032021.4326.3). Residual differential phase interferograms were spatially filtered using a Goldstein filter with 0.6 strength to reduce the impact of decorrelation during phase unwrapping. Also, to minimise negative impacts during phase unwrapping, pixels located in the sea were masked to zero using a fine-resolution coastline. Unwrapping was carried out using a minimum cost flow algorithm. All interferograms were cropped to a common area and georeferenced to the UTM zone 26S coordinate system.

2. Seismic catalogue and relocation

Seismic waveform data

There are two permanent seismic networks in the Azores (codes: PM, CP)[93–95], operated by IPMA and CIVISA, respectively, with five stations on São Jorge before the start of the 2022 unrest. On 23 March 2022, just four days after the start of the seismic swarm, 15 temporary short-period seismic stations were installed (code: 3K). Three temporary broadband stations were installed four days later (code: PM). An additional 10 broadband stations were installed on São Jorge and adjacent islands in June 2022 (code: 8S)[96]. Finally, at the end of August 2022, we deployed six short-period ocean bottom seismometers (OBSs) offshore São Jorge[97]. In this study, we analyse available seismic data until 18 November 2022, covering the first eight months of the seismic swarm.

Seismic catalogue generation workflow

We developed a fully automated workflow to detect, pick, and associate seismic arrivals. For most of the studied period, we used the EQTransformer convolutional neural network model[98] implemented in SeisBench[99], to detect and pick *P*- and *S*-wave arrivals. The association step was performed using

PyOcto[100]. For the OBS deployment period, we found that an existing neural network trained on OBSs[101] yielded many false picks, producing many false associations. Therefore, for this latter period, we used QuakeMigrate [102], which back-projects characteristic functions of the seismic waveforms, to a coherent source, thus implicitly associating picked arrival times with events.

This workflow yielded 11,968 well-located events (maximum azimuthal gap ≤ 220°; ≥8 arrival times) relocated in an initial velocity model based on Rayleigh wave ellipticities recorded at PM.ROSA in the west of São Jorge[46] (Fig. S6). We generated 5,000 random realisations of this starting model, perturbing velocities up to 2 km/s) and layer thicknesses (ensuring a minimum thickness of 0.5 km and maximum thickness of 4 km), jointly inverting for velocity structure and hypocentres[103–105]. We chose the best-fitting output model as our preferred, minimum 1-D velocity structure (Fig. S6).

NLL-SSST-coherence relocation method

Initial locations using an inverted 1-D velocity model (Fig. S6) show a highly clustered swarm, however, the relatively large uncertainty in the absolute hypocentre positions (median depth uncertainty of 430 m) indicates that greater precision is needed. Moreover, the evolving station density during the 2022 São Jorge seismic swarm, with sparse station coverage for the first few days necessitates a joint earthquake relocation approach that couples station corrections and relative locations between the later and earlier periods. We, therefore, used a new, multi-scale high-precision method, *NLL-SSST-coherence*[106,107], which combines source-specific station travel-time corrections (SSSTs) to account for 3-D velocity heterogeneity, with the stacking of hypocentre probability density functions based on inter-event waveform coherence to improve smaller-scale relative location. We computed inter-event waveform coherency using a 2-40 Hz bandpass filter.

The workflow of NLL-SSST-coherence comprises a two-step process. First, SSSTs to our best-fitting 1-D velocity model (Fig. S6) are developed iteratively over collapsing length scales, using well-constrained events with at least 15 arrival times. Next, assuming that highly similar waveforms for two events recorded at the same station imply the events are nearly co-located, we measure inter-event waveform coherency at multiple stations as a weight to combine and stack the location probability density functions from the NLL-SSST relocations. This approach effectively reduces stochastic noise in travel-time data, greatly improving the location precision of target events. The practical advantages of this approach are that it only requires waveforms for a few stations and is computationally fast compared to other more high-precision relative location algorithms, such as hypoDD and GrowClust because differential arrival time measurements do not need to be computed. NLL-SSST-coherence produces high location precision across multiple scales, leading to a different interpretation of seismicity patterns than with methods that focus on fine-scale precision[106]. NLL-SSST-coherence has been applied to volcano-tectonic seismicity in other areas[108].

Frequency-magnitude relationships

Caution is needed when interpreting *b*-values from frequency-magnitude distributions using local magnitude (M_L) scales of low-magnitude seismic sequences[109–114]. These studies show that moment magnitude (M_w) gives more accurate b-value estimates; therefore, we computed M_w using S_H-wave spectra[115,116]. We found that compared to *P*-wave spectra, M_w estimates from S_H-wave spectra had smaller uncertainties, had a greater number of good spectral fits, and had a stronger correlation with the corresponding initial M_L.

For computing *b*-values, we computed the magnitude of completeness (M_c) using the boundary-value-stability method[54,68,114,117].

Focal mechanisms

We computed focal mechanisms using Bayesian inversion of first-motion polarity data[118]. All solutions were best fit by double-couple mechanisms. An example solution is shown in Fig. S8.

3. GNSS processing

Daily Solutions

The daily positions of each station were estimated using the GipsyX software package[119], employing the Precise Point Positioning (PPP) strategy[120]. This approach allows for the independent computation of station positions by relying on fixed satellite orbit and clock parameters provided by the Jet Propulsion Laboratory (JPL). To ensure alignment within the latest realisation of the International Terrestrial Reference System, the ITRF2020 reference frame, daily transformation parameters estimated by JPL were applied. For earlier solutions where ITRF2020 transformation parameters were unavailable, existing solutions in ITRF2014 were converted to ITRF2020 using global parameters provided by the International Terrestrial Reference Frame service (https://itrf.ign.fr/).

Time-series Analysis

The long-term motion of each GNSS station was analysed using the Hector software package[121], specifically designed for time series analysis of geodetic data. The trajectory of each station was modelled as a combination of a linear trend (secular motion), seasonal signals (annual and semi-annual variations), and step offsets caused by geophysical or instrumental changes.

Outlier detection and removal were performed as an initial step using an automated approach[122]. To ensure realistic uncertainty estimates for the derived parameters, Hector accounts for temporal correlations in the GNSS time series. A noise model consisting of a power-law component combined with white noise was employed, as this has been shown to accurately represent the noise characteristics of geodetic data. The software estimates not only the linear velocity but also the amplitudes and phase-lags of seasonal signals.

Offsets in the data, resulting from events such as equipment changes, antenna replacements, or geophysical phenomena, were systematically incorporated into the model to ensure accurate estimation of the motion for all stations. For the deformation caused by the dike intrusion, offsets were computed to quantify the sudden displacements observed at the start of the swarm on 19 March 2022. To isolate these displacements, one week of GNSS data around this epoch was excluded from the analysis for all stations. This exclusion minimised the influence of short-term noise and allowed for the precise computation of the deformation signals related to the dike intrusion.

4. Mechanical modelling of surface displacement observations

The surface displacements observed by the GNSS network and Sentinel-1A interferograms show evidence of a major island axis elongated dilatation source in the central-west area of São Jorge. This pattern is characteristic of magmatic intrusions, typically a nearly vertical dike. To quantify the dimensions and magma volume associated with this intrusive pattern, we utilised a 3D Mixed Boundary Element Method[123]. The model assumes that the volcanic island edifice and upper crust are homogeneous, and isotropic and behave elastically with a Young's modulus of 5 GPa and a Poisson's ratio of 0.25. The 3D BEM method is a flexible numerical approach accounting for topography/bathymetry and non-planar dilatant cracks (e.g., quadrangles).

To account for a realistic topography, we created a blended topography and bathymetry model at 100 m spatial resolution combining the GLO30 COPERNICUS model for the island's topography and the 2023 version of the EMODnet bathymetry model for the Azores (EMODnet DTM 2022).

We explore models of planar quadrangular intrusions allowing for tilted (inwards or outwards) crack boundaries along depth. First, the inversion explores nonlinear geometry parameters followed by the solution of the crack opening which satisfies constant overpressure, by linear inversion. Note that a single magma overpressure parameter controls the dike opening pattern. This physically realistic assumption produces spatially smooth opening distributions, independent of the chosen crack mesh discretisation, and avoids setting up a linear inversion regularisation smoothing parameter (typical for kinematic inversions).

The inversion iteratively explores a large set of model parameters describing the dike intrusion position, orientation and dimensions by generating forward models optimised by a neighbourhood inversion algorithm[124,125]. These models minimise the misfit with the observed displacements between the 15 and 21 March 2022. To carry out the inversions in an efficient manner, the spatial resolution of the surface displacement maps was reduced using a quadtree partition approach with a minimum average quadrant size of 8 pixels and a maximum of 128 pixels, to subdivide the quadrants two conditions were specified: displacement variance and displacement thresholds both of 0.03 m. These parameters result in the selection of 698 and 702 points for the descending and ascending interferograms, respectively. We used all three component GNSS vectors. During the inversion, the weights of the three types of observations were normalised to avoid results being dominated by a single dataset.

Forward modelling tests

To explore the scenario of a laterally migrating dyke, we forward-modelled intrusion scenarios through the seismicity region with a range of dike opening models with random (20,000 samples) geometries/sizes using parameters from the solution space of the geodetic inversion. We found that most models produce a surface displacement signal that would be resolvable with the GNSS network in São Jorge or InSAR data but that we do not observe (Fig. S15). Only very small intrusions, with <100-to-1000 m^3 of magma, would have been missed by GNSS (<1 mm) and InSAR (<1 cm). Therefore, we can likely rule out laterally propagating dike fingers hundreds of metres to ~2 km wide in depth.

5. Auto-correlation imaging

The ACF approach has been successfully used to image temporal variations in subsurface structure beneath volcanic regions[126–128]. The phase autocorrelation method is not biased by high amplitude features such as earthquakes and thus does not require pre-processing (e.g., normalisation) to remove these features[129–131]. We tested different frequency bands and found that the 1.0-3.0 Hz band gave the most stable results, and is lower than most of the radiation from events of the seismic swarm. We also tested three different stacking windows, with and without overlap, and obtained consistent results. The ACF were computed as 3-day linear stacks with a 2-day overlap.

Acknowledgements

We are grateful to the UK Ocean Bottom Instrument Consortium (OBIC) and SEIS-UK teams for providing the instrumentation and installation services. A.M.G.F, R.R., and N.M. received urgency funding from the Natural Environment Research Council (NE/X006298/1). A.M.G.F. also acknowledges funding from the European Research Council (101001601). This work was also supported by Portuguese FCT/MCTES through national funds (PIDDAC), namely through projects GEMMA (PTDC/CTA-GEO/2083/2021), RESTLESS (PTDC/CTA-GEF/6674/2020, DOI: 10.54499/PTDC/CTA-GEF/6674/2020), UIDB/04683/2020 (DOI: 10.54499/UIDB/04683/2020), and UIDP/04683/2020 (DOI: 10.54499/UIDP/04683/2020), and the Spanish Ministry of Science, Innovation and Universities VolcaMotion project (*Proyecto* PID2022-139159NB-I00 *financiado por MCIN/AEI/10.13039/501100011033/ y por FEDER Una manera de hacer Europa*). A.P. acknowledges the CEEC Institutional contract funded by FCT (DOI: 10.54499/CEECINST/00024/2021/CP2780/CT0003). The Portuguese Navy (Marinha Portuguesa) is acknowledged for providing critical support in the deployment and recovery of the OBS network; we particularly thank the captain and crews of NRPs *António Enes* and *Sines*. The Azores Government, through its Fundo Regional para a Ciência, is also acknowledged for its financial support to harbour operations during the deployment and recovery of the OBS network. We thank Paula Lourinho, Filipe Porteiro and Octávio Melo from OKEANOS, University of the Azores, Sandra Sequeira from Observatório Príncipe Alberto do Mónaco (IPMA) in Faial, José Silva (Serviço de Ambiente e Ação Climática de São Jorge / Parque Natural de São Jorge) and Miguel Mendonça (Municipality of Angra do Heroísmo), for crucial logistics support for both the OBS and land deployments. We thank CAD team from CIVISA for collecting and processing seismic data. We thank Luis Matias (IDL and the University of Lisbon) and Thomas Boulesteix (IPNA-CSIC) for fruitful discussions.

Data and Code availability

Seismic waveform data from the PM network are available from the IPMA FDSN webservices client at http://ceida.ipma.pt/. Waveform data from temporary networks 8S and 4U are archived at the Earthscope Data Management Center (http://ds.iris.edu) and are under embargo until 2026-01-01.

Our seismicity catalogue and 1-D layered velocity model is available from a Zenodo repository[132].

The Sentinel-1A IW SLCs and satellite orbits files used in this study are provided by the European Space Agency (ESA) and files are publically available through the Alaska Satellite Facility (ASF) Data Search Vertex (https://search.asf.alaska.edu). Bathymetry data around the Azores from the EMODnet Digital Bathymetry [133], while topography on land was obtained from the COPERNICUS GLO-30

Global Digital Elevation Model (https://portal.opentopography.org/raster?opentopoID=OTSDEM.032021.4326.3).

The GNSS daily files for the stations used in this study are available at the Portuguese GNSS National Repository managed by the Collaboratory for Geosciences (https://glass.c4g-pt.eu/) maintained with the support of EPOS (European Plate Observing System) (https://www.epos-eu.org/). The analysed stations belong to different networks: QEMD, HORT, PIED, AZTP, AZGR, TERC are part of the REPRAA network (https://repraa.azores.gov.pt/); ENAO is part of the IGS network (https://igs.org); and VLAZ and PAGU are part of the the C4G network (https://glass.c4g-pt.eu/).

Geodetic inverse models were conducted using the DefVolc software, which is available online at the http://opgc.fr/defvolc website. Displacements, strains and stresses from triangular dislocations were computed using cutde (https://github.com/tbenthompson/cutde).

Author contributions

Conceptualization: SPH, PJG, AMGF, RSR, NM

Methodology: SPH, PJG, AL, AMGF, RSR

Software: SPH, PJG, AL, GS

Validation: SPH, PJG, GS

Formal analysis: SPH, PJG, AL, RSR

Investigation: SPH, PJG, AMGF, RSR, NM, GS, NAF, JF, RF, AP, MT, VM, RS, WS, AM, FC, RM, MM, GP

Data Curation: SPH, AMGF, NAD, RF, MT, VM, RS, AP, WS, AM, FC, RM

Writing - Original Draft: SPH, PJG, AMGF, RSR, NM

Writing - Review & Editing: SPH, PJG, AL, AMGF, RSR, NM, GS, NAD, JF, RF, AP, SC, RM, VM, WS, RM, GP

Visualisation: SPH, PJG, AL, RSR, GS

Supervision: AMGF

Project administration: SPH, PJG, AMGF

Funding acquisition: AMGF, RSR, NM, RF, PJG, RM, SC, NAD

References

1. Moran, S. C., Newhall, C. & Roman, D. C. Failed magmatic eruptions: late-stage cessation of magma ascent. *Bull. Volcanol.* **73**, 115–122 (2011).
2. Rubin, A. M. Dike-induced faulting and graben subsidence in volcanic rift zones. *J. Geophys. Res. Solid Earth* **97**, 1839–1858 (1992).
3. Lejeune, A. M., Bottinga, Y., Trull, T. W. & Richet, P. Rheology of bubble-bearing magmas. *Earth Planet. Sci. Lett.* **166**, 71–84 (1999).
4. Gaffney, E. S., Damjanac, B. & Valentine, G. A. Localization of volcanic activity: 2. Effects of pre-existing structure. *Earth Planet. Sci. Lett.* **263**, 323–338 (2007).
5. Gudmundsson, A. Form and dimensions of dykes in eastern Iceland. *Tectonophysics* **95**, 295–307 (1983).
6. Sigmundsson, F. *et al.* Fracturing and tectonic stress drives ultrarapid magma flow into dikes. *Science* **0**, eadn2838 (2024).
7. Ziv, A., Rubin, A. M. & Agnon, A. Stability of dike intrusion along preexisting fractures. *J. Geophys. Res. Solid Earth* **105**, 5947–5961 (2000).
8. Maccaferri, F., Rivalta, E., Passarelli, L. & Aoki, Y. On the mechanisms governing dike arrest: Insight from the 2000 Miyakejima dike injection. *Earth Planet. Sci. Lett.* **434**, 64–74 (2016).
9. Bangs, N. L. B., Shipley, T. H., Moore, J. C. & Moore, G. F. Fluid accumulation and channeling along the northern Barbados Ridge decollement thrust. *J. Geophys. Res. Solid Earth* **104**, 20399–20414 (1999).
10. Caricchi, L., Townsend, M., Rivalta, E. & Namiki, A. The build-up and triggers of volcanic eruptions. *Nat. Rev. Earth Environ.* **2**, 458–476 (2021).
11. Ross, Z. E., Cochran, E. S., Trugman, D. T. & Smith, J. D. 3D fault architecture controls the dynamism of earthquake swarms. *Science* **368**, 1357–1361 (2020).
12. Roman, D. C. Numerical models of volcanotectonic earthquake triggering on non-ideally oriented faults. *Geophys. Res. Lett.* **32**, (2005).
13. Manga, M. & Brodsky, E. Seismic Triggering of Eruptions in the Far Field: Volcanoes and Geysers.

Annu. Rev. Earth Planet. Sci. **34**, 263–291 (2006).

14. Roman, D. C. & Heron, P. Effect of regional tectonic setting on local fault response to episodes of volcanic activity. *Geophys. Res. Lett.* **34**, (2007).
15. Toda, S., Stein, R. S. & Sagiya, T. Evidence from the ad 2000 Izu islands earthquake swarm that stressing rate governs seismicity. *Nature* **419**, 58–61 (2002).
16. White, R. S., Edmonds, M., Maclennan, J., Greenfield, T. & Agustsdottir, T. Melt movement through the Icelandic crust. *Philos. Trans. R. Soc. Math. Phys. Eng. Sci.* **377**, 20180010 (2019).
17. Wilding, J. D., Zhu, W., Ross, Z. E. & Jackson, J. M. The magmatic web beneath Hawaiʻi. *Science* **379**, 462–468 (2023).
18. Einarsson, P., Hjartardóttir, Á. R., Hreinsdóttir, S. & Imsland, P. The structure of seismogenic strike-slip faults in the eastern part of the Reykjanes Peninsula Oblique Rift, SW Iceland. *J. Volcanol. Geotherm. Res.* **391**, 106372 (2020).
19. Drymoni, K., Browning, J. & Gudmundsson, A. Volcanotectonic interactions between inclined sheets, dykes, and faults at the Santorini Volcano, Greece. *J. Volcanol. Geotherm. Res.* **416**, 107294 (2021).
20. Trippanera, D. *et al.* Relationships between tectonics and magmatism in a transtensive/transform setting: An example from Faial Island (Azores, Portugal). *GSA Bull.* **126**, 164–181 (2014).
21. Hildenbrand, A. *et al.* Multi-stage evolution of a sub-aerial volcanic ridge over the last 1.3 Myr: S. Jorge Island, Azores Triple Junction. *Earth Planet. Sci. Lett.* **273**, 289–298 (2008).
22. DeMets, C., Gordon, R. G. & Argus, D. F. Geologically current plate motions. *Geophys. J. Int.* **181**, 1–80 (2010).
23. Mendes, V. B. *et al.* Present-day deformation in São Jorge Island, Azores, from episodic GPS measurements (2001–2011). *Adv. Space Res.* **51**, 1581–1592 (2013).
24. Marques, F. O., Hildenbrand, A. & Hübscher, C. Evolution of a volcanic island on the shoulder of an oceanic rift and geodynamic implications: S. Jorge Island on the Terceira Rift, Azores Triple Junction. *Tectonophysics* **738–739**, 41–50 (2018).

25. Lourenço, N. *et al.* Morpho-tectonic analysis of the Azores Volcanic Plateau from a new bathymetric compilation of the area. *Mar. Geophys. Res.* **20**, 141–156 (1998).
26. Borges, J. F., Bezzeghoud, M., Buforn, E., Pro, C. & Fitas, A. The 1980, 1997 and 1998 Azores earthquakes and some seismo-tectonic implications. *Tectonophysics* **435**, 37–54 (2007).
27. Ekström, G., Nettles, M. & Dziewoński, A. M. The global CMT project 2004–2010: Centroid-moment tensors for 13,017 earthquakes. *Phys. Earth Planet. Inter.* **200–201**, 1–9 (2012).
28. Frietsch, M., Ferreira, A., Vales, D. & Carrilho, F. On the robustness of seismic moment tensor inversions for mid-ocean earthquakes: the Azores archipelago. *Geophys. J. Int.* **215**, 564–584 (2018).
29. Madeira, J. & Ribeiro, A. Geodynamic models for the Azores triple junction: A contribution from tectonics. *Tectonophysics* **184**, 405–415 (1990).
30. Silva, P. F. *et al.* Palaeomagnetic study of a subaerial volcanic ridge (São Jorge Island, Azores) for the past 1.3 Myr: evidence for the Cobb Mountain Subchron, volcano flank instability and tectonomagmatic implications. *Geophys. J. Int.* **188**, 959–978 (2012).
31. Neves, M. C., Miranda, J. M. & Luis, J. F. The role of lithospheric processes on the development of linear volcanic ridges in the Azores. *Tectonophysics* **608**, 376–388 (2013).
32. Moreira, M. A., Geoffroy, L. & Pozzi, J. P. Magma flow pattern in dykes of the Azores revealed by anisotropy of magnetic susceptibility. *J. Geophys. Res. Solid Earth* **120**, 662–690 (2015).
33. Marques, F. O., Catalão, J. C., DeMets, C., Costa, A. C. G. & Hildenbrand, A. GPS and tectonic evidence for a diffuse plate boundary at the Azores Triple Junction. *Earth Planet. Sci. Lett.* **381**, 177–187 (2013).
34. Madeira, J., Brum da Silveira, A., Hipólito, A. & Carmo, R. Chapter 3 Active tectonics in the central and eastern Azores islands along the Eurasia–Nubia boundary: a review. *Geol. Soc. Lond. Mem.* **44**, 15–32 (2015).
35. Miranda, J. M., Luis, J. F., Lourenço, N. & Goslin, J. Distributed deformation close to the Azores Triple “Point”. *Mar. Geol.* **355**, 27–35 (2014).

36. Marzoli, A. *et al.* Time-Dependent Evolution and Source Heterogeneities of Ocean Island Basalts from a Weak Plume, São Jorge, Azores. *J. Petrol.* egae122 (2024) doi:10.1093/petrology/egae122.
37. Forjaz, V. H. & Weston, F. S. Volcanic activity in the Azores. Report for 1959–1964. *Bull. Volcanol.* **31**, 261–266 (1967).
38. Gaspar, J. L. *et al.* Chapter 4 Earthquakes and volcanic eruptions in the Azores region: geodynamic implications from major historical events and instrumental seismicity. *Geol. Soc. Lond. Mem.* **44**, 33–49 (2015).
39. Fontiela, J., Sousa Oliveira, C. & Rosset, P. Characterisation of Seismicity of the Azores Archipelago: An Overview of Historical Events and a Detailed Analysis for the Period 2000–2012. in *Volcanoes of the Azores: Revealing the Geological Secrets of the Central Northern Atlantic Islands* (eds. Kueppers, U. & Beier, C.) 127–153 (Springer, Berlin, Heidelberg, 2018). doi:10.1007/978-3-642-32226-6_8.
40. Silva, R., Carmo, R. & Marques, R. Characterization of the tectonic origins of historical and modern seismic events and their societal impact on the Azores Archipelago, Portugal. in *Characterization of Modern and Historical Seismic–Tsunamic Events, and Their Global–Societal Impacts* (eds. Dilek, Y., Ogawa, Y. & Okubo, Y.) 0 (Geological Society of London, 2021). doi:10.1144/SP501-2019-106.
41. Machado, F. O terramoto de S. Jorge, em 1757. *Açoreana* **4**, 311–324 (1949).
42. Madeira, J. & Brum da Silveira, A. Active tectonics and first paleoseismological results in Faial, Picoand S. Jorge islands (Azores, Portugal). (2003).
43. Asensio-Ramos, M. *et al.* Soil He and H2 degassing during the recent seismic crisis of São Jorge Island, Azores. EGU-6185 (2023) doi:10.5194/egusphere-egu23-6185.
44. Suarez, E. D. *et al.* São Jorge's Volcano-Tectonic Unrest in 2022: A Joint Interpretation Through GNSS and Fully Automated Seismic Analysis. *Pure Appl. Geophys.* (2024) doi:10.1007/s00024-024-03612-y.
45. Spieker, K., Rondenay, S., Ramalho, R., Thomas, C. & Helffrich, G. Constraints on the structure of

the crust and lithosphere beneath the Azores Islands from teleseismic receiver functions. *Geophys. J. Int.* **213**, 824–835 (2018).

46. Ferreira, A. M. G., Marignier, A., Attanayake, J., Frietsch, M. & Berbellini, A. Crustal structure of the Azores Archipelago from Rayleigh wave ellipticity data. *Geophys. J. Int.* **221**, 1232–1247 (2020).
47. Bondár, I. & Storchak, D. Improved location procedures at the International Seismological Centre: Improved location procedures at the ISC. *Geophys. J. Int.* **186**, 1220–1244 (2011).
48. Chamberlain, C. J. *et al.* EQcorrscan: Repeating and Near-Repeating Earthquake Detection and Analysis in Python. *Seismol. Res. Lett.* **89**, 173–181 (2017).
49. Schimmel, M. *et al.* Seismic Noise Autocorrelations on Mars. *Earth Space Sci.* **8**, e2021EA001755 (2021).
50. Zanon, V., Pimentel, A., Auxerre, M., Marchini, G. & Stuart, F. M. Unravelling the magma feeding system of a young basaltic oceanic volcano. *Lithos* **352–353**, 105325 (2020).
51. Zanon, V., Silva, R. & Goulart, C. The crust-mantle transition beneath the Azores region (central-north Atlantic Ocean). *Contrib. Mineral. Petrol.* **178**, 50 (2023).
52. Leva, C., Rümpker, G., Link, F. & Wölbern, I. Mantle earthquakes beneath Fogo volcano, Cape Verde: Evidence for subcrustal fracturing induced by magmatic injection. *J. Volcanol. Geotherm. Res.* **386**, 106672 (2019).
53. Torres-González, P. A. *et al.* Unrest signals after 46 years of quiescence at Cumbre Vieja, La Palma, Canary Islands. *J. Volcanol. Geotherm. Res.* **392**, 106757 (2020).
54. Greenfield, T. *et al.* Deep long period seismicity preceding and during the 2021 Fagradalsfjall eruption, Iceland. *Bull. Volcanol.* **84**, 101 (2022).
55. Hudson, T. S. *et al.* Deep crustal melt plumbing of Bárðarbunga volcano, Iceland. *Geophys. Res. Lett.* **44**, 8785–8794 (2017).
56. del Fresno, C. *et al.* Magmatic plumbing and dynamic evolution of the 2021 La Palma eruption. *Nat. Commun.* **14**, 358 (2023).
57. Roman, D. C. & Cashman, K. V. Top–Down Precursory Volcanic Seismicity: Implications for

‘Stealth’ Magma Ascent and Long-Term Eruption Forecasting. *Front. Earth Sci.* **6**, (2018).

58. Maccaferri, F., Bonafede, M. & Rivalta, E. A quantitative study of the mechanisms governing dike propagation, dike arrest and sill formation. *J. Volcanol. Geotherm. Res.* **208**, 39–50 (2011).
59. Pinel, V. & Jaupart, C. Magma storage and horizontal dyke injection beneath a volcanic edifice. *Earth Planet. Sci. Lett.* **221**, 245–262 (2004).
60. Yamaoka, K., Kawamura, M., Kimata, F., Fujii, N. & Kudo, T. Dike intrusion associated with the 2000 eruption of Miyakejima Volcano, Japan. *Bull. Volcanol.* **67**, 231–242 (2005).
61. Ebinger, C. J. *et al.* Capturing magma intrusion and faulting processes during continental rupture: Seismicity of the Dabbahu (Afar) rift. *Geophys. J. Int.* **174**, 1138–1152 (2008).
62. Keir, D. *et al.* Evidence for focused magmatic accretion at segment centers from lateral dike injections captured beneath the Red Sea rift in Afar. *Geology* **37**, 59–62 (2009).
63. Pallister, J. S. *et al.* Broad accommodation of rift-related extension recorded by dyke intrusion in Saudi Arabia. *Nat. Geosci.* **3**, 705–712 (2010).
64. White, R. S. *et al.* Dynamics of dyke intrusion in the mid-crust of Iceland. *Earth Planet. Sci. Lett.* **304**, 300–312 (2011).
65. Woods, J., Winder, T., White, R. S. & Brandsdóttir, B. Evolution of a lateral dike intrusion revealed by relatively-relocated dike-induced earthquakes: The 2014–15 Bárðarbunga–Holuhraun rifting event, Iceland. *Earth Planet. Sci. Lett.* **506**, 53–63 (2019).
66. Cesca, S. *et al.* Massive earthquake swarm driven by magmatic intrusion at the Bransfield Strait, Antarctica. *Commun. Earth Environ.* **3**, 1–11 (2022).
67. Sigmundsson, F. *et al.* Deformation and seismicity decline before the 2021 Fagradalsfjall eruption. *Nature* **609**, 523–528 (2022).
68. Roberts, N. S., Bell, A. F. & Main, I. G. Are volcanic seismic *b*-values high, and if so when? *J. Volcanol. Geotherm. Res.* **308**, 127–141 (2015).
69. Kettlety, T., Kendall, J. M. & Roman, D. C. Self-Similarity of Seismic Moment Release to Volume Change Scaling for Volcanoes: A Comparison With Injection-Induced Seismicity. *Geophys. Res. Lett.* **49**, e2022GL099369 (2022).

70. Glazner, A. F. & McNutt, S. R. Relationship Between Dike Injection and b-Value for Volcanic Earthquake Swarms. *J. Geophys. Res. Solid Earth* **126**, e2020JB021631 (2021).
71. Wyss, M., Shimazaki, K. & Wiemer, S. Mapping active magma chambers by b values beneath the off-Ito volcano, Japan. *J. Geophys. Res. Solid Earth* **102**, 20413–20422 (1997).
72. Meyer, K., Biggs, J. & Aspinall, W. A Bayesian reassessment of the relationship between seismic moment and magmatic intrusion volume during volcanic unrest. *J. Volcanol. Geotherm. Res.* **419**, 107375 (2021).
73. Di Luccio, F. *et al.* Seismic signature of active intrusions in mountain chains. *Sci. Adv.* **4**, e1701825 (2018).
74. Wilding, J. D. & Ross, Z. E. Rift Zone Architecture and Inflation-Driven Seismicity of Mauna Loa Volcano. *J. Geophys. Res. Solid Earth* **129**, e2024JB029726 (2024).
75. Schofield, N. J., Brown, D. J., Magee, C. & Stevenson, C. T. Sill morphology and comparison of brittle and non-brittle emplacement mechanisms. *J. Geol. Soc.* **169**, 127–141 (2012).
76. Elsworth, D. & Voight, B. Dike intrusion as a trigger for large earthquakes and the failure of volcano flanks. *J. Geophys. Res. Solid Earth* **100**, 6005–6024 (1995).
77. Roman, D. C. & Cashman, K. V. The origin of volcano-tectonic earthquake swarms. *Geology* **34**, 457–460 (2006).
78. Martens, H. R. & White, R. S. Triggering of microearthquakes in Iceland by volatiles released from a dyke intrusion. *Geophys. J. Int.* **194**, 1738–1754 (2013).
79. Coulon, C. A., Hsieh, P. A., White, R., Lowenstern, J. B. & Ingebritsen, S. E. Causes of distal volcano-tectonic seismicity inferred from hydrothermal modeling. *J. Volcanol. Geotherm. Res.* **345**, 98–108 (2017).
80. Wicks, C. W., Dzurisin, D., Lowenstern, J. B. & Svarc, J. Magma Intrusion and Volatile Ascent Beneath Norris Geyser Basin, Yellowstone National Park. *J. Geophys. Res. Solid Earth* **125**, e2019JB018208 (2020).
81. Díaz-Moreno, A. *et al.* Seismic hydraulic fracture migration originated by successive deep magma pulses: The 2011–2013 seismic series associated to the volcanic activity of El Hierro

Island. *J. Geophys. Res. Solid Earth* **120**, 7749–7770 (2015).

82. Métrich, N. *et al.* Is the 'Azores Hotspot' a Wetspot? Insights from the Geochemistry of Fluid and Melt Inclusions in Olivine of Pico Basalts. *J. Petrol.* **55**, 377–393 (2014).
83. Dixon, J. E., Stolper, E. M. & Holloway, J. R. An Experimental Study of Water and Carbon Dioxide Solubilities in Mid-Ocean Ridge Basaltic Liquids. Part I: Calibration and Solubility Models. *J. Petrol.* **36**, 1607–1631 (1995).
84. Vargas-Bracamontes, D. M. & Neuberg, J. W. Interaction between regional and magma-induced stresses and their impact on volcano-tectonic seismicity. *J. Volcanol. Geotherm. Res.* **243–244**, 91–96 (2012).
85. Roman, D. C., Soldati, A., Dingwell, D. B., Houghton, B. F. & Shiro, B. R. Earthquakes indicated magma viscosity during Kīlauea's 2018 eruption. *Nature* **592**, 237–241 (2021).
86. Rubin, A. M. & Gillard, D. Dike-induced earthquakes: Theoretical considerations. *J. Geophys. Res. Solid Earth* **103**, 10017–10030 (1998).
87. Harris, R. A. Large earthquakes and creeping faults. *Rev. Geophys.* **55**, 169–198 (2017).
88. Gillard, D., Rubin, A. M. & Okubo, P. Highly concentrated seismicity caused by deformation of Kilauea's deep magma system. *Nature* **384**, 343–346 (1996).
89. Phillips, T. B., Magee, C., Jackson, C. A.-L. & Bell, R. E. Determining the three-dimensional geometry of a dike swarm and its impact on later rift geometry using seismic reflection data. *Geology* **46**, 119–122 (2017).
90. McGarr, A. Maximum magnitude earthquakes induced by fluid injection. *J. Geophys. Res. Solid Earth* **119**, 1008–1019 (2014).
91. González, P. J. Interferometric Synthetic Aperture Radar (InSAR). in *Remote Sensing for Characterization of Geohazards and Natural Resources* (eds. Chaussard, E., Jones, C., Chen, J. A. & Donnellan, A.) 53–73 (Springer International Publishing, Cham, 2024). doi:10.1007/978-3-031-59306-2_3.
92. Hogenson, K. *et al.* Hybrid Pluggable Processing Pipeline (HyP3): A cloud-native infrastructure for generic processing of SAR data. Zenodo https://doi.org/10.5281/ZENODO.4646138 (2024).

93. Instituto Português do Mar e da Atmosfera (IPMA). Portuguese National Seismic Network. International Federation of Digital Seismograph Networks https://doi.org/10.7914/SN/PM (2006).

94. Carrilho, F. *et al.* The Portuguese National Seismic Network—Products and Services. *Seismol. Res. Lett.* **92**, 1541–1570 (2021).

95. Centro do Informação e Vigilância Sismovulcânica dos Açores, U. O. A. CIVISA Seismo-Volcanic Monitoring Network-Azores Islands. Approximately 2 active stations Deutsches GeoForschungsZentrum GFZ https://doi.org/10.14470/PC311625 (2021).

96. Ferreira, A. M. G., Ramalho, R. D. S. & Mitchell, N. Azores Network. 81000 MB International Federation of Digital Seismograph Networks https://doi.org/10.7914/FGP0-C809 (2026).

97. Ferreira, A. M. G., Mitchell, N., Ramalho, R. D. S., Hicks, S. & Tsekhmistrenko, M. São Jorge OBS Network. 115000 MB International Federation of Digital Seismograph Networks https://doi.org/10.7914/D5W4-V395 (2026).

98. Mousavi, S. M., Ellsworth, W. L., Zhu, W., Chuang, L. Y. & Beroza, G. C. Earthquake transformer—an attentive deep-learning model for simultaneous earthquake detection and phase picking. *Nat. Commun.* **11**, 3952 (2020).

99. Woollam, J. *et al.* SeisBench—A Toolbox for Machine Learning in Seismology. *Seismol. Res. Lett.* **93**, 1695–1709 (2022).

100. Münchmeyer, J. PyOcto: A high-throughput seismic phase associator. *Seismica* **3**, (2024).

101. Bornstein, T. *et al.* PickBlue: Seismic Phase Picking for Ocean Bottom Seismometers With Deep Learning. *Earth Space Sci.* **11**, e2023EA003332 (2024).

102. Winder, T. *et al. QuakeMigrate: A Modular, Open-Source Python Package for Automatic Earthquake Detection and Location*. https://essopenarchive.org/doi/full/10.1002/essoar.10505850.1 (2021) doi:10.1002/essoar.10505850.1.

103. Kissling, E., Ellsworth, W. L., Eberhart-Phillips, D. & Kradolfer, U. Initial reference models in local earthquake tomography. *J. Geophys. Res. Solid Earth* **99**, 19635–19646 (1994).

104. Hicks, S. P., Rietbrock, A., Ryder, I. M., Lee, C.-S. & Miller, M. Anatomy of a megathrust: The 2010

M8. 8 Maule, Chile earthquake rupture zone imaged using seismic tomography. *Earth Planet. Sci. Lett.* **405**, 142–155 (2014).

105. Bie, L. *et al.* Along‐Arc Heterogeneity in Local Seismicity across the Lesser Antilles Subduction Zone from a Dense Ocean‐Bottom Seismometer Network. *Seismol. Res. Lett.* **91**, 237–247 (2020).
106. Lomax, A. & Henry, P. Major California faults are smooth across multiple scales at seismogenic depth. *Seismica* **2**, (2023).
107. Lomax, A. & Savvaidis, A. High-Precision Earthquake Location Using Source-Specific Station Terms and Inter-Event Waveform Similarity. *J. Geophys. Res. Solid Earth* **127**, e2021JB023190 (2022).
108. Lomax, A., Tuvè, T., Giampiccolo, E. & Cocina, O. A new view of seismicity under Mt. Etna volcano, Italy, 2014-2023 from multi-scale high-precision earthquake relocations. *Ann. Geophys.* **67**, S437–S437 (2024).
109. Ross, Z. E., Ben-Zion, Y., White, M. C. & Vernon, F. L. Analysis of earthquake body wave spectra for potency and magnitude values: implications for magnitude scaling relations. *Geophys. J. Int.* **207**, 1158–1164 (2016).
110. Deichmann, N. Theoretical Basis for the Observed Break in ML/Mw Scaling between Small and Large Earthquakes. *Bull. Seismol. Soc. Am.* **107**, 505–520 (2017).
111. Staudenmaier, N., Tormann, T., Edwards, B., Deichmann, N. & Wiemer, S. Bilinearity in the Gutenberg-Richter Relation Based on ML for Magnitudes Above and Below 2, From Systematic Magnitude Assessments in Parkfield (California). *Geophys. Res. Lett.* **45**, 6887–6897 (2018).
112. Hicks, S. P. *et al.* A Shallow Earthquake Swarm Close to Hydrocarbon Activities: Discriminating between Natural and Induced Causes for the 2018–2019 Surrey, United Kingdom, Earthquake Sequence. *Seismol. Res. Lett.* **90**, 2095–2110 (2019).
113. Lanza, F., Thurber, C. H., Syracuse, E. M., Power, J. A. & Ghosh, A. Seismic tomography of compressional wave velocity and attenuation structure for Makushin Volcano, Alaska. *J. Volcanol. Geotherm. Res.* **393**, 106804 (2020).

114. Hudson, T. S., Kendall, J.-M., Pritchard, M. E., Blundy, J. D. & Gottsmann, J. H. From slab to surface: Earthquake evidence for fluid migration at Uturuncu volcano, Bolivia. *Earth Planet. Sci. Lett.* **577**, 117268 (2022).

115. Satriano, C. SourceSpec – Earthquake source parameters from P- or S-wave displacement spectra. Zenodo https://doi.org/10.5281/zenodo.6954238 (2022).

116. Hicks, S. P. *et al.* Slab to back-arc to arc: Fluid and melt pathways through the mantle wedge beneath the Lesser Antilles. *Sci. Adv.* **9**, eadd2143 (2023).

117. Cao, A. & Gao, S. S. Temporal variation of seismic b-values beneath northeastern Japan island arc. *Geophys. Res. Lett.* **29**, 48-1-48–3 (2002).

118. Pugh, D. J. & White, R. S. MTfit: A Bayesian Approach to Seismic Moment Tensor Inversion. *Seismol. Res. Lett.* **89**, 1507–1513 (2018).

119. Bertiger, W. *et al.* GipsyX/RTGx, a new tool set for space geodetic operations and research. *Adv. Space Res.* **66**, 469–489 (2020).

120. Zumberge, J. F., Heflin, M. B., Jefferson, D. C., Watkins, M. M. & Webb, F. H. Precise point positioning for the efficient and robust analysis of GPS data from large networks. *J. Geophys. Res. Solid Earth* **102**, 5005–5017 (1997).

121. Bos, M. S., Araujo, I. & Bastos, B. L. Hector user manual version 1.1. (2013).

122. Fernandes, R. M. S. & Bos, M. S. Applied automatic offset detection using HECTOR within EPOS-IP. **2016**, G51A-1084 (2016).

123. Cayol, V. & Cornet, F. H. 3D mixed boundary elements for elastostatic deformation field analysis. *Int. J. Rock Mech. Min. Sci.* **34**, 275–287 (1997).

124. Sambridge, M. Geophysical inversion with a neighbourhood algorithm—I. Searching a parameter space. *Geophys. J. Int.* **138**, 479–494 (1999).

125. Fukushima, Y., Cayol, V. & Durand, P. Finding realistic dike models from interferometric synthetic aperture radar data: The February 2000 eruption at Piton de la Fournaise. *J. Geophys. Res. Solid Earth* **110**, 2004JB003268 (2005).

126. Yukutake, Y., Ueno, T. & Miyaoka, K. Determination of temporal changes in seismic velocity

caused by volcanic activity in and around Hakone volcano, central Japan, using ambient seismic noise records. *Prog. Earth Planet. Sci.* **3**, 29 (2016).

127. De Plaen, R. S. M. *et al.* Temporal Changes of Seismic Velocity Caused by Volcanic Activity at Mt. Etna Revealed by the Autocorrelation of Ambient Seismic Noise. *Front. Earth Sci.* **6**, (2019).
128. Wu, S.-M. *et al.* Spatiotemporal Seismic Structure Variations Associated With the 2018 Kīlauea Eruption Based on Temporary Dense Geophone Arrays. *Geophys. Res. Lett.* **47**, e2019GL086668 (2020).
129. Schimmel, M., Stutzmann, E. & Gallart, J. Using instantaneous phase coherence for signal extraction from ambient noise data at a local to a global scale. *Geophys. J. Int.* **184**, 494–506 (2011).
130. Schimmel, M., Stutzmann, E. & Ventosa, S. Low‐Frequency Ambient Noise Autocorrelations: Waveforms and Normal Modes. *Seismol. Res. Lett.* **89**, 1488–1496 (2018).
131. Sánchez-Pastor, P., Obermann, A. & Schimmel, M. Detecting and Locating Precursory Signals During the 2011 El Hierro, Canary Islands, Submarine Eruption. *Geophys. Res. Lett.* **45**, 10,288-10,297 (2018).
132. Hicks, S. Supplementary data for ‘Leaky faults modulated magma ascent and adjacent seismicity during the 2022 São Jorge Island (Azores) seismic-volcanic unrest’ by Hicks, Gonzalez, et al. Zenodo https://doi.org/10.5281/zenodo.14421663 (2024).
133. EMODnet Bathymetry Consortium. EMODnet Digital Bathymetry (DTM 2022). EMODnet Bathymetry Consortium https://doi.org/10.12770/FF3AFF8A-CFF1-44A3-A2C8-1910BF109F85 (2022).

Supplementary Material

to

Leaky faults modulated magma ascent and adjacent seismicity during the 2022 São Jorge Island (Azores) seismic-volcanic unrest

by Stephen P. Hicks, Pablo J. Gonzalez, *et al.*

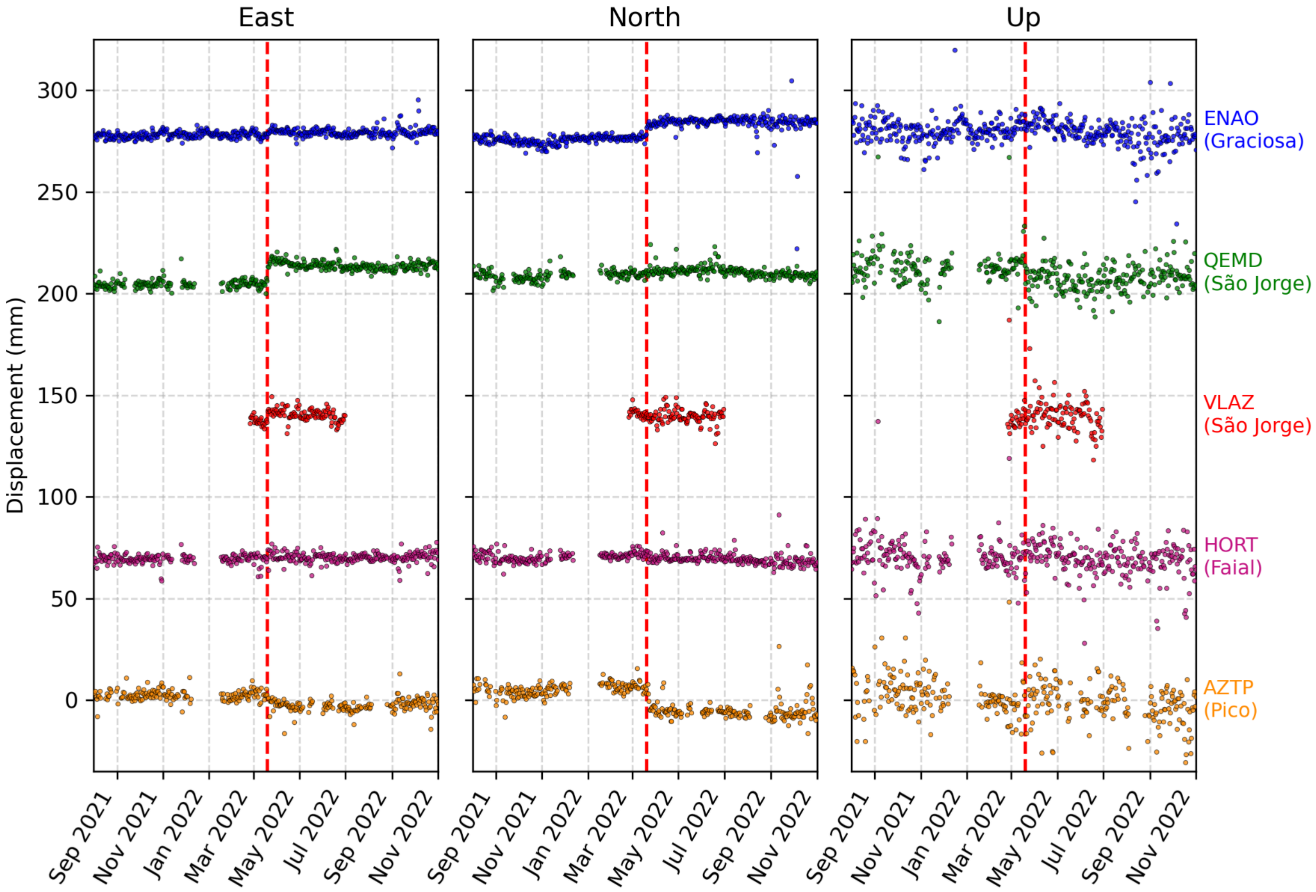

Fig. S1: *East (left), north (middle), and vertical (right) daily GNSS displacements from stations across the Central Group of the Azores (Fig. 1b). Stations are ordered from north (top) to south (bottom). Displacements are within a global reference frame, with the secular trend removed. The vertical red dashed line shows the onset of the seismic crisis.*

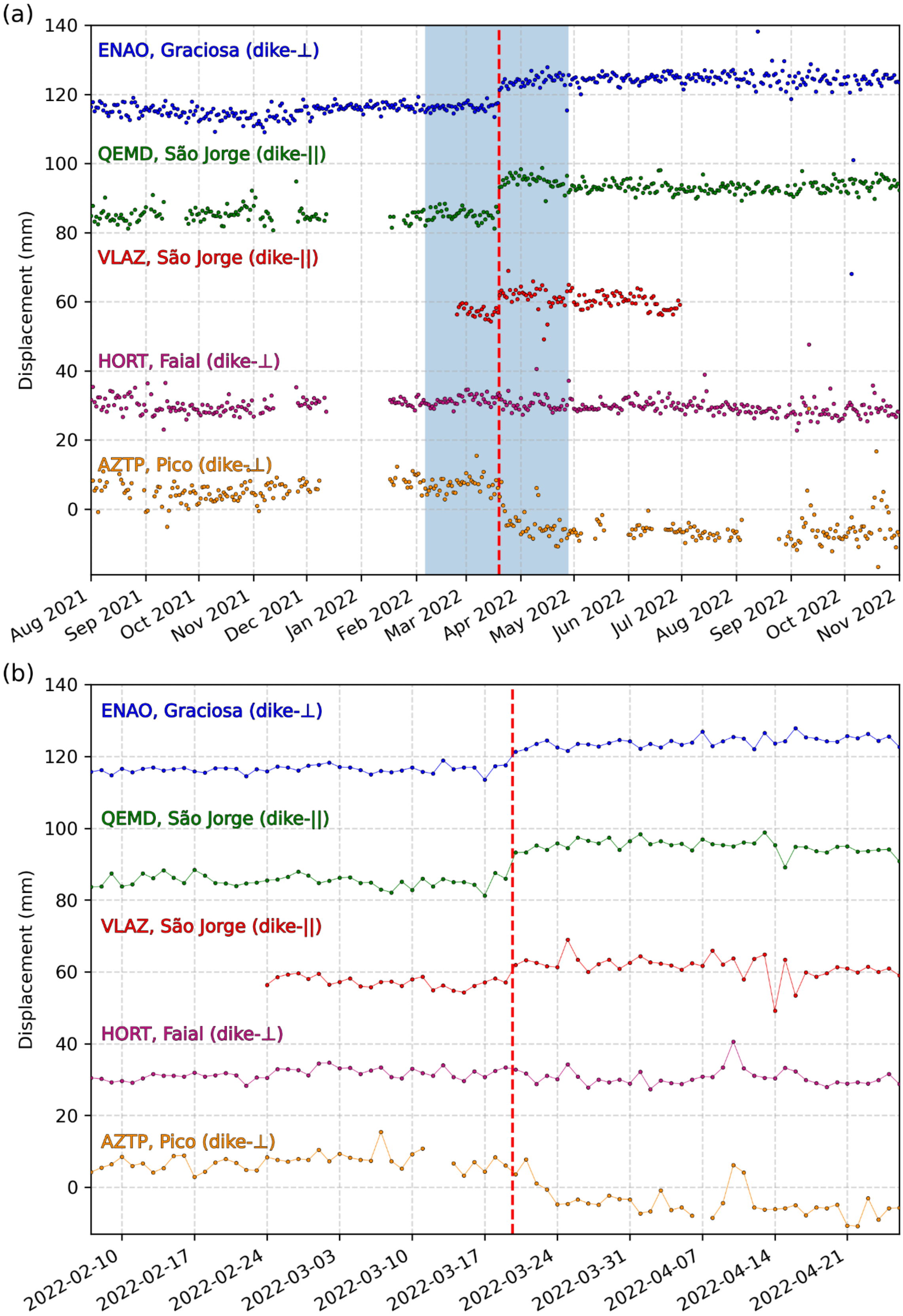

Fig. S2: *Daily GNSS displacements from stations across the Central Group of the Azores (Fig. 1b). Stations are ordered from north (top) to south (bottom). Displacements are within a global reference frame, with the secular trend removed. Horizontal displacements have been rotated into a reference frame relative to the strike of the modelled dike intrusion (285°): dike-parallel (||) and dike-perpendicular (⊥) displacements. The vertical red dashed line shows the onset of the seismic crisis. The blue shaded area in (a) denotes the time window of the zoomed-in view in (b).*

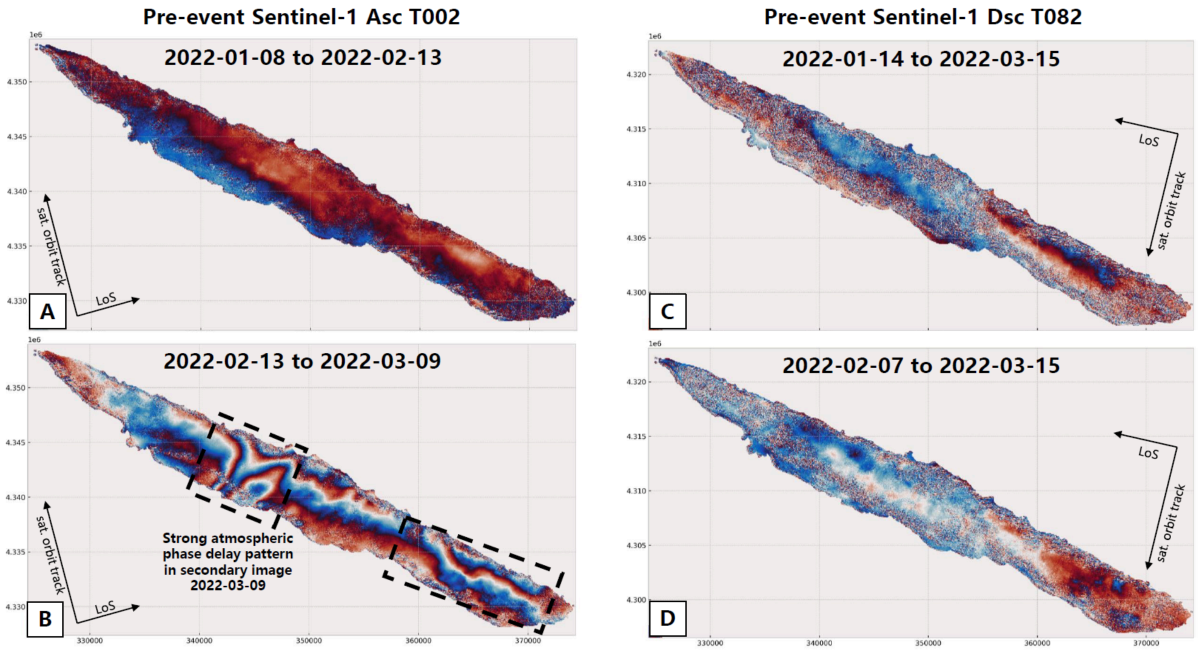

Fig. S3: *Wrapped phase (C-band) ascending (A and B panels) and descending (C and D panels) Sentinel-1A interferograms from before the onset of seismicity showing that there were no InSAR detectable displacements (> 1 cm) before 15 March 2022 in São Jorge. Note that Panel B shows a strong phase pattern in the area of maximum co-diking displacements; however, pair-wise comparisons with multiple interferograms indicate that this phase delay pattern is likely a strong atmospheric phase delay affecting the 9 March 2022 radar image, as demonstrated by Panel D which spans a similar period.*

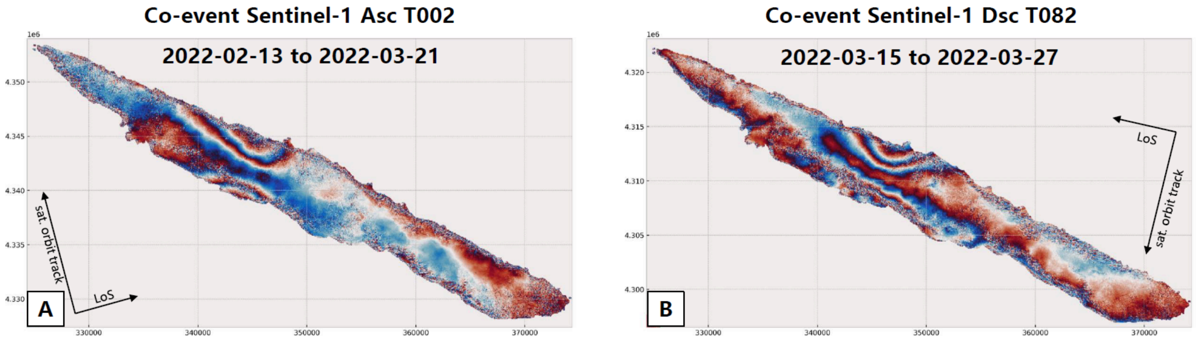

Fig. S4: *Wrapped phase (C-band) ascending (A; same as Fig. 1c) and descending (B) Sentinel-1A co-onset of seismicity interferograms, showing that both, ascending and descending, pairs detected displacements with similar amplitude indicating that most of the deformation occurred between 15 March 2022 and 21 March 2022 in São Jorge.*

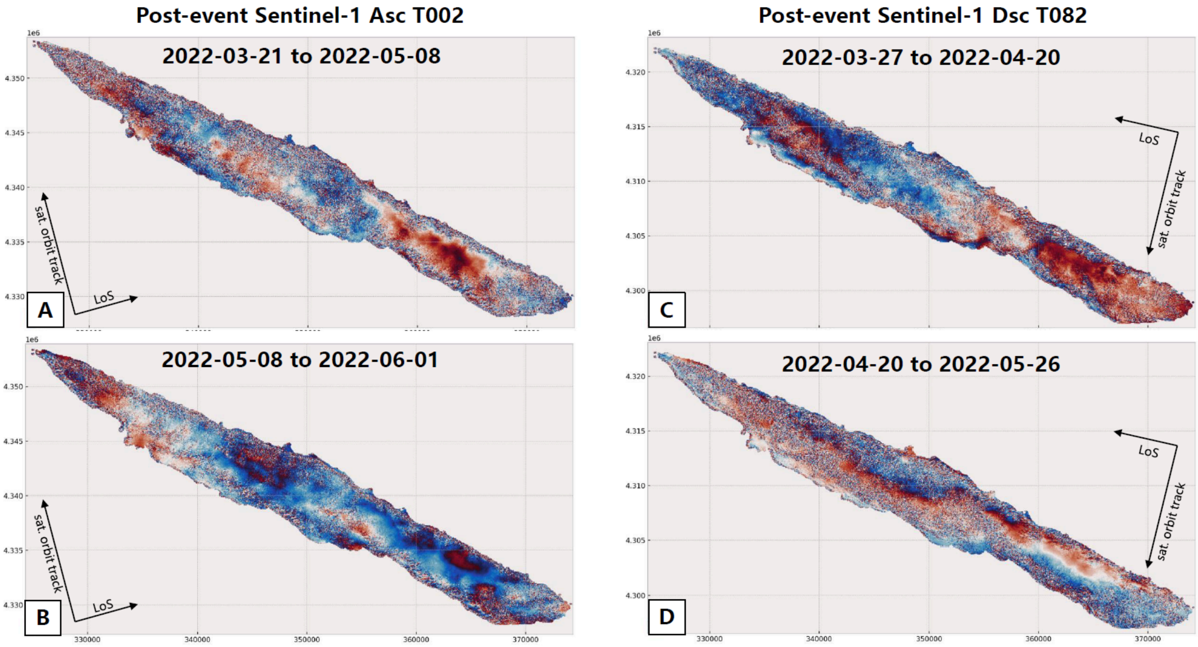

Fig. S5: *Wrapped phase (C-band) ascending (A and B panels) and descending (C and D panels) Sentinel-1A post-onset of seismicity interferograms, showing that there were no InSAR detectable displacements (> 1 cm) after 21 March 2022 in São Jorge.*

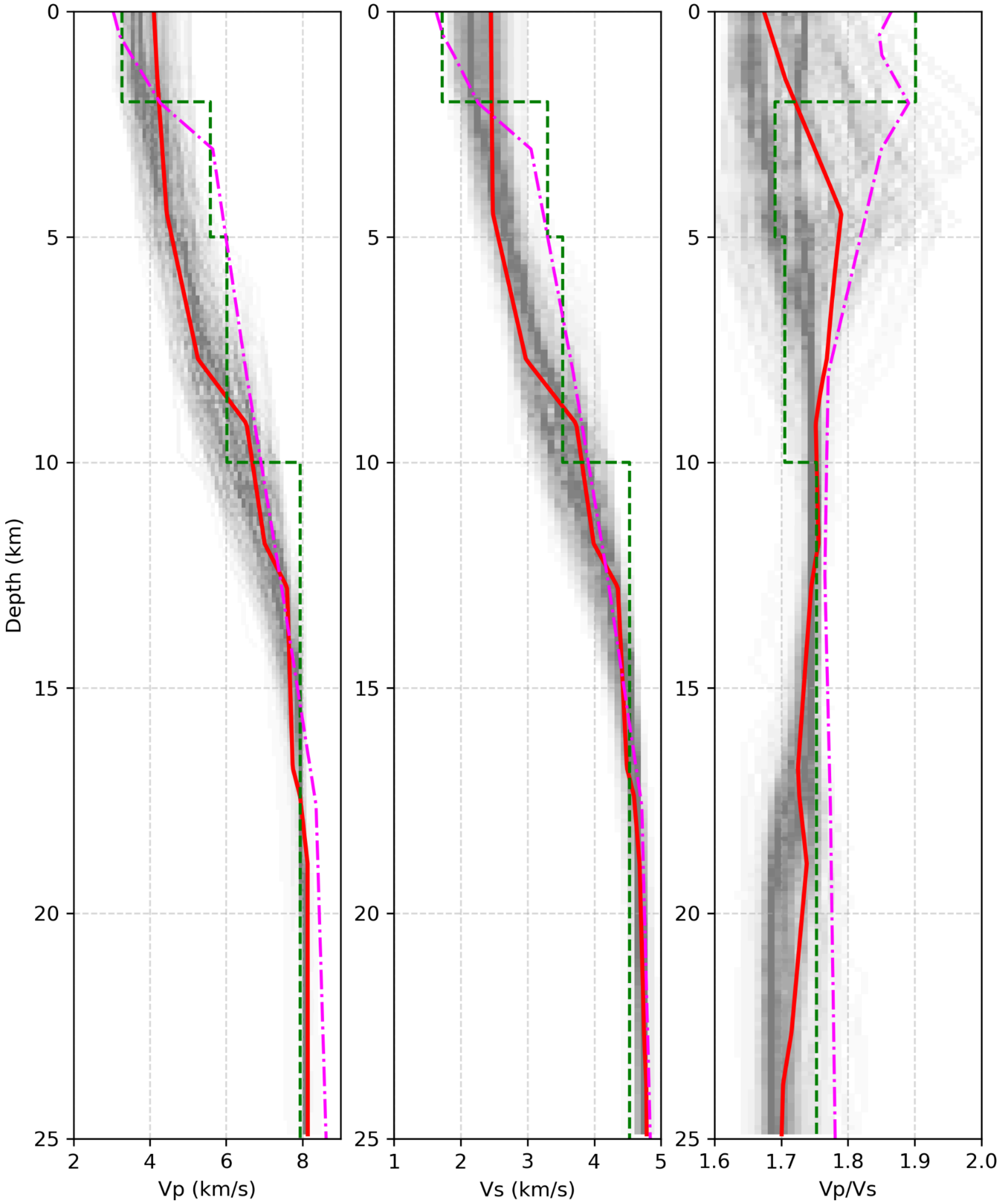

Fig. S6: *Minimum 1-D velocity model. Left: P-wave velocity; middle: S-wave velocity; right: v_p/v_s ratio. The red line shows the model with the lowest RMS misfit to arrival time observations. The grey shading shows the range of inverted models that have an RMS misfit within 5% of the best-fitting model. The green dashed line shows the layered model previously obtained by Ferreira et al.*[1] *using Rayleigh wave ellipticity measurements from station PM.ROSA, located on the west of São Jorge (Fig. 1b) The magenta dash-dotted was derived using local earthquake arrival times for the Faial-Pico region of the Central Islands of the Azores*[2]

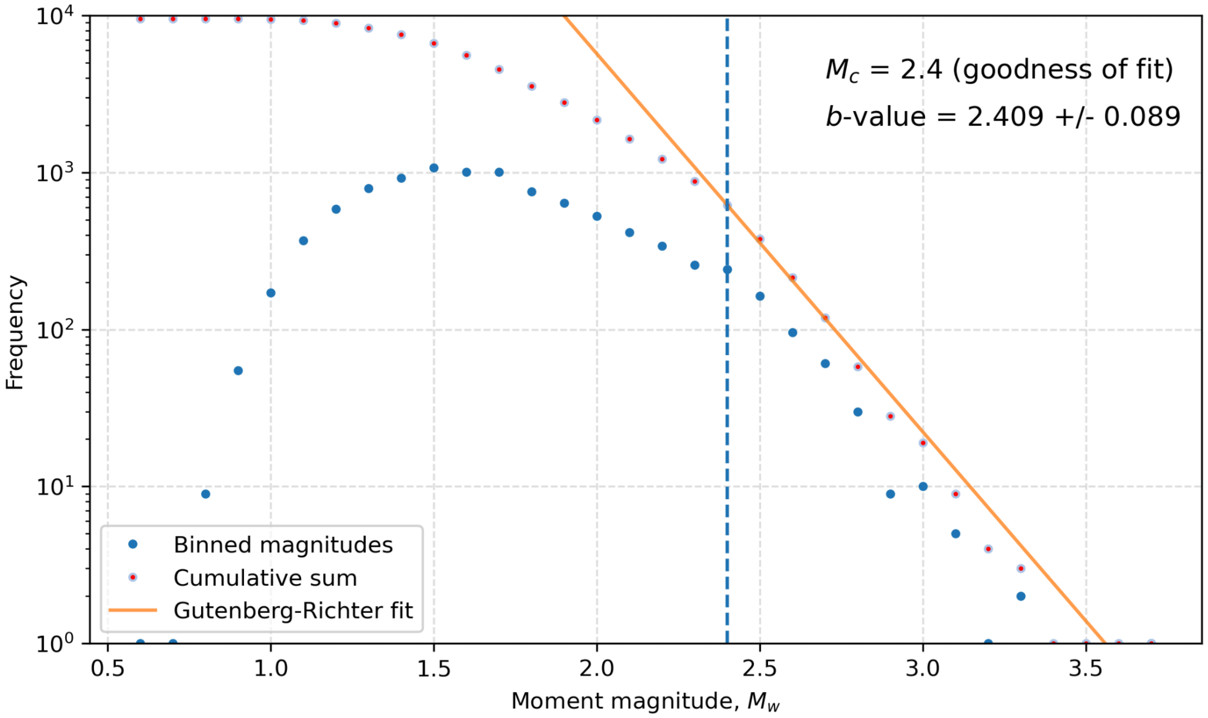

Fig S7: *Overall catalogue frequency-magnitude distribution showing computed b-value and magnitude of completeness (M_c) from moment magnitude estimates, computed using the boundary-value-stability method*[3].

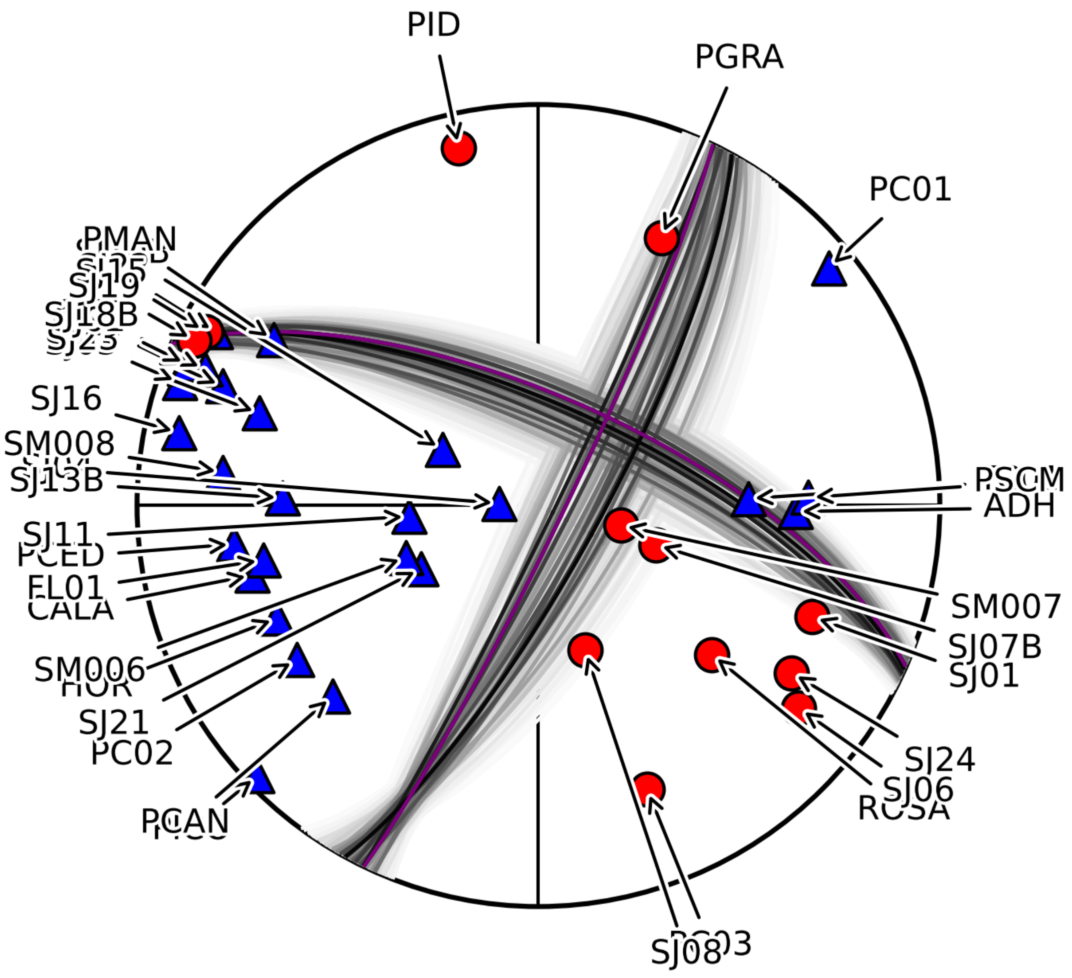

Fig S8: *Example of a tightly constrained earthquake focal mechanism based on P-wave polarities. The event had an origin time of 28/07/2022 20:51:23, a depth of 10.2 km, and a moment magnitude of 2.88. Red circles are compressional first motions; blue triangles are dilatational. The range of possible solutions is given by black lines, with the best-fitting solution in purple.*

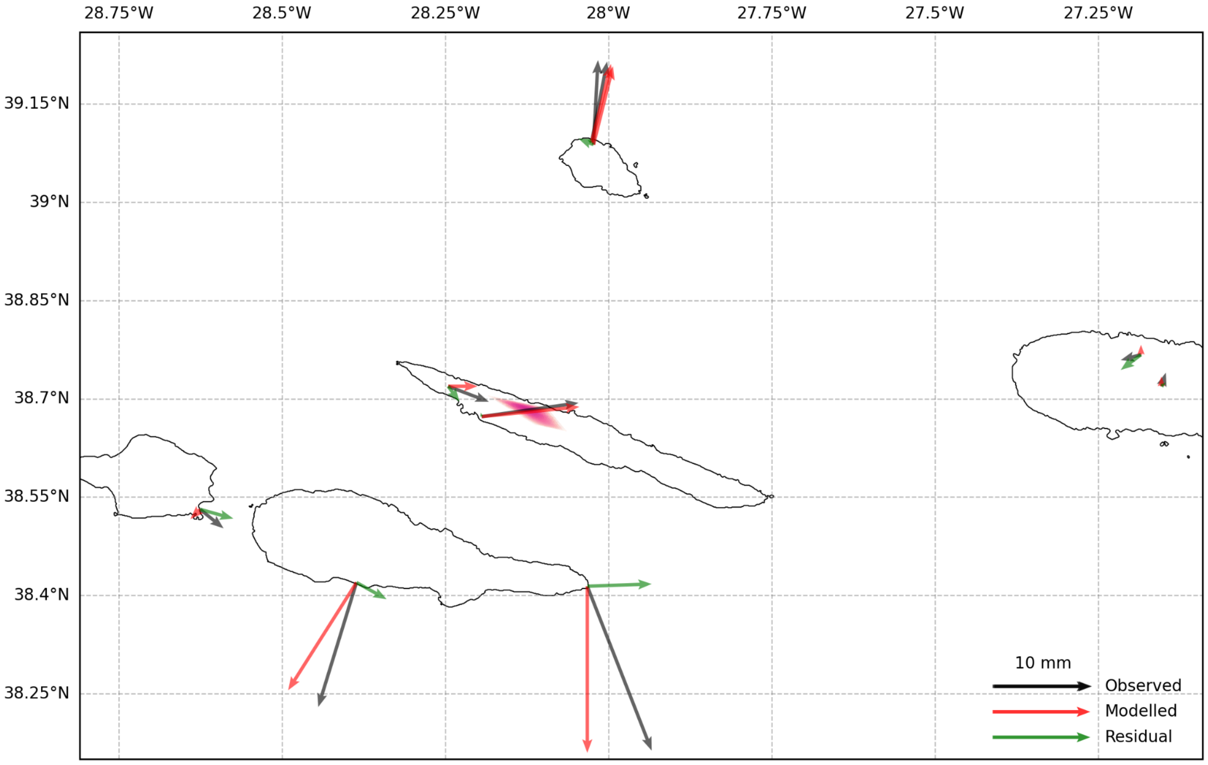

Fig S9: *Observed, predicted, and residual GNSS horizontal displacement vectors from our joint BEM dike intrusion model. The dike intrusion is shown in purple.*

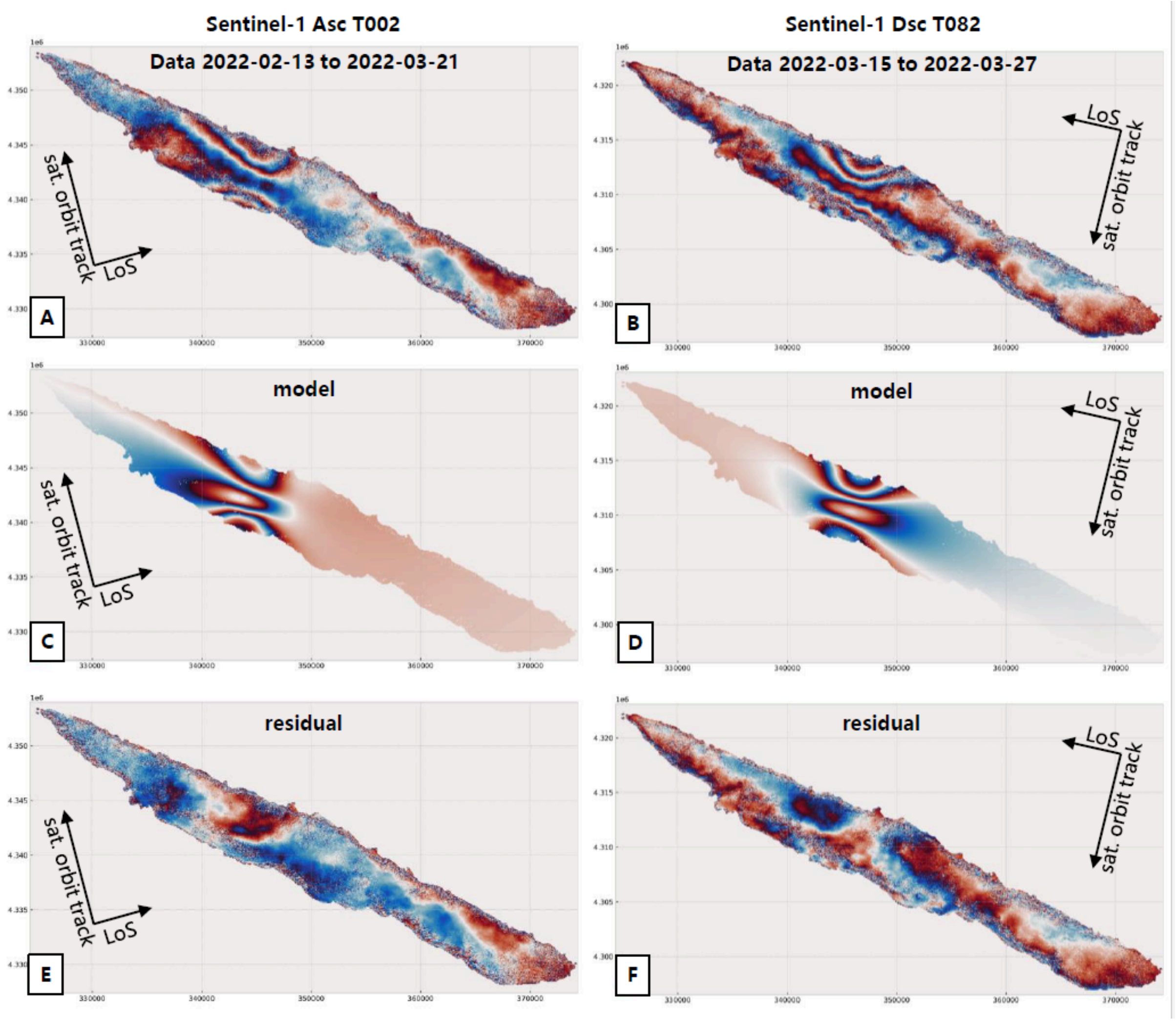

Fig S10: *Ascending and descending (re-wrapped phase) InSAR displacement (A and B panels), model prediction (C and D panels) and residual (E and F panels) maps for São Jorge Island from our joint GNSS and InSAR inversion BEM dike intrusion model, including realistic topography-bathymetry.*

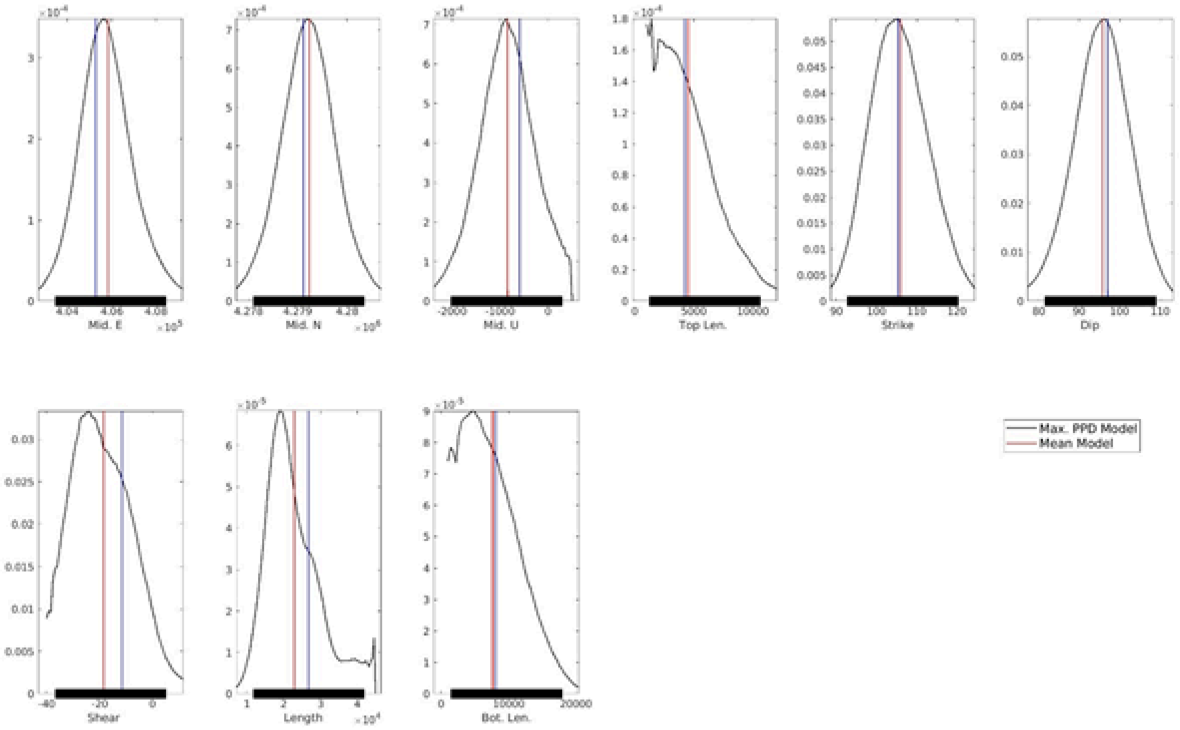

Fig. S11. *Marginal probability density functions of the inverted parameters of the GNSS vectors and ascending and descending InSAR displacement maps constrained quadrangle dike model.*

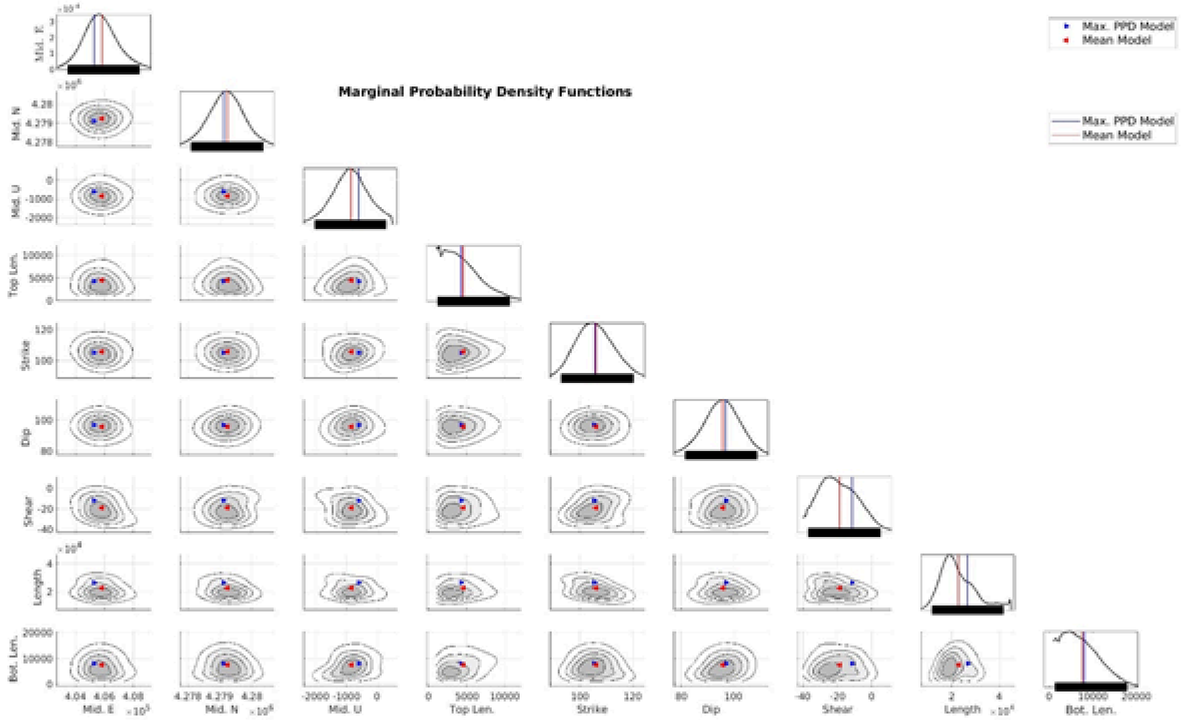

Fig. S12. *2D Marginal probability density functions of the inverted parameters of the GNSS vectors and ascending and descending InSAR displacement maps constrained quadrangle dike model. Circular 2D distributions show that the parameter spaces were well sampled and no strong trade-off correlations affect the inverted model parameter results.*

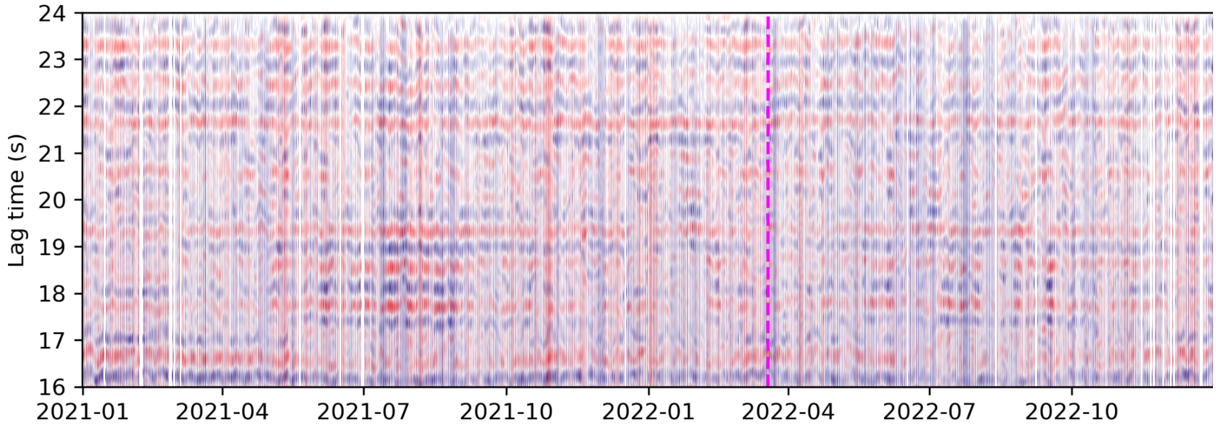

Fig. S13: *Same as Fig. 3d, but instead showing the results from station PM.ROSA.*

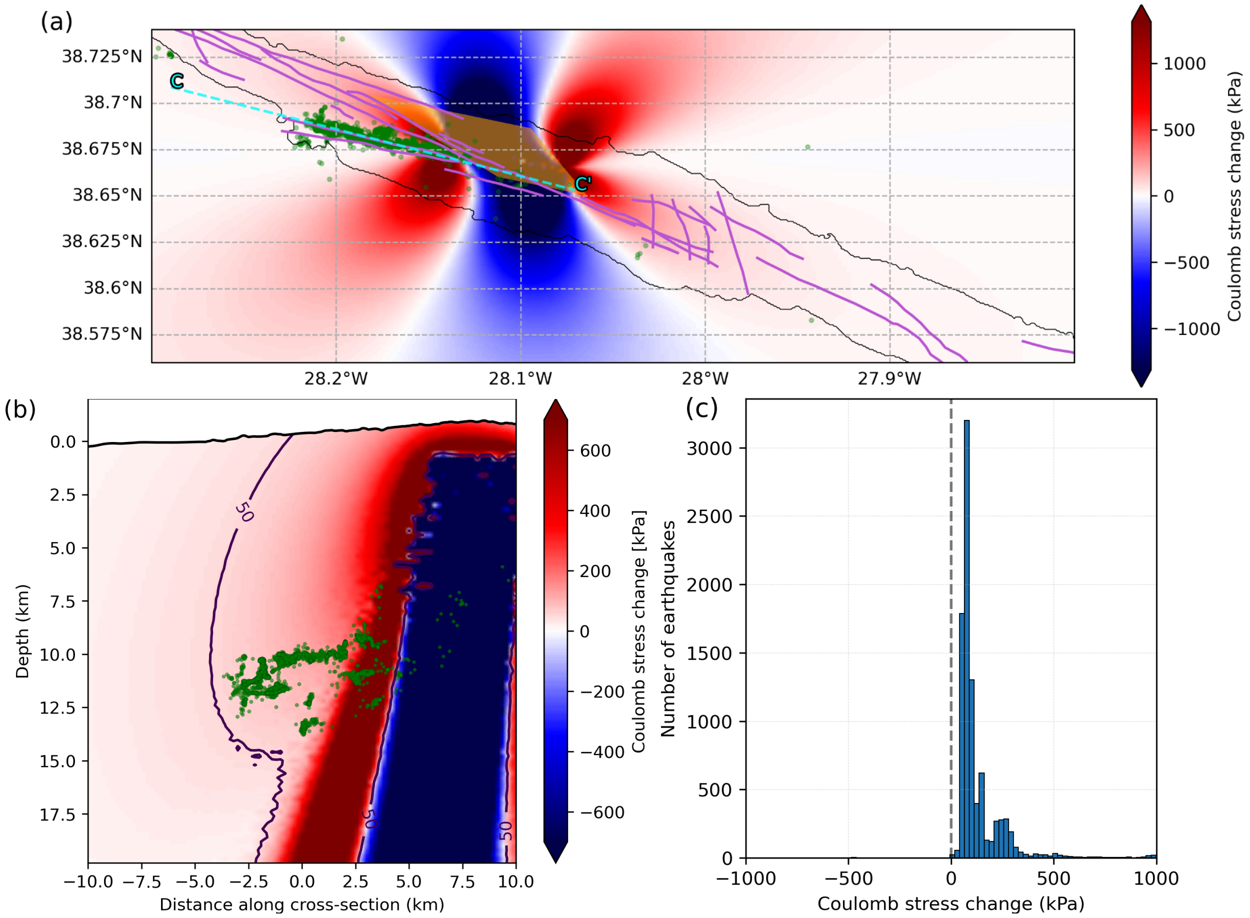

***Fig. S14**. Coulomb stress analysis due to the modelled dike intrusion. a) Map showing the Coulomb stress change at 10.5 km depth (the mean depth of seismicity), based on vertical-dipping left-lateral (0° rake) receiver faults striking 280° (as indicated by the seismicity locations and focal mechanisms). Pink lines are mapped fault traces; green circles are the relocated seismicity epicentres; orange shading is the modelled dike intrusion. b) Same as (a), with the model plotted along a cross-section striking parallel to the main seismicity lineation. c) Histogram showing the computed Coulomb stress at each earthquake hypocentre. The median value is 87 kPa. d) Coulomb stress computed on mapped receiver faults at the surface, assuming a vertical dip and pure left-lateral slip (0° rake) at 10.5 km depth.*

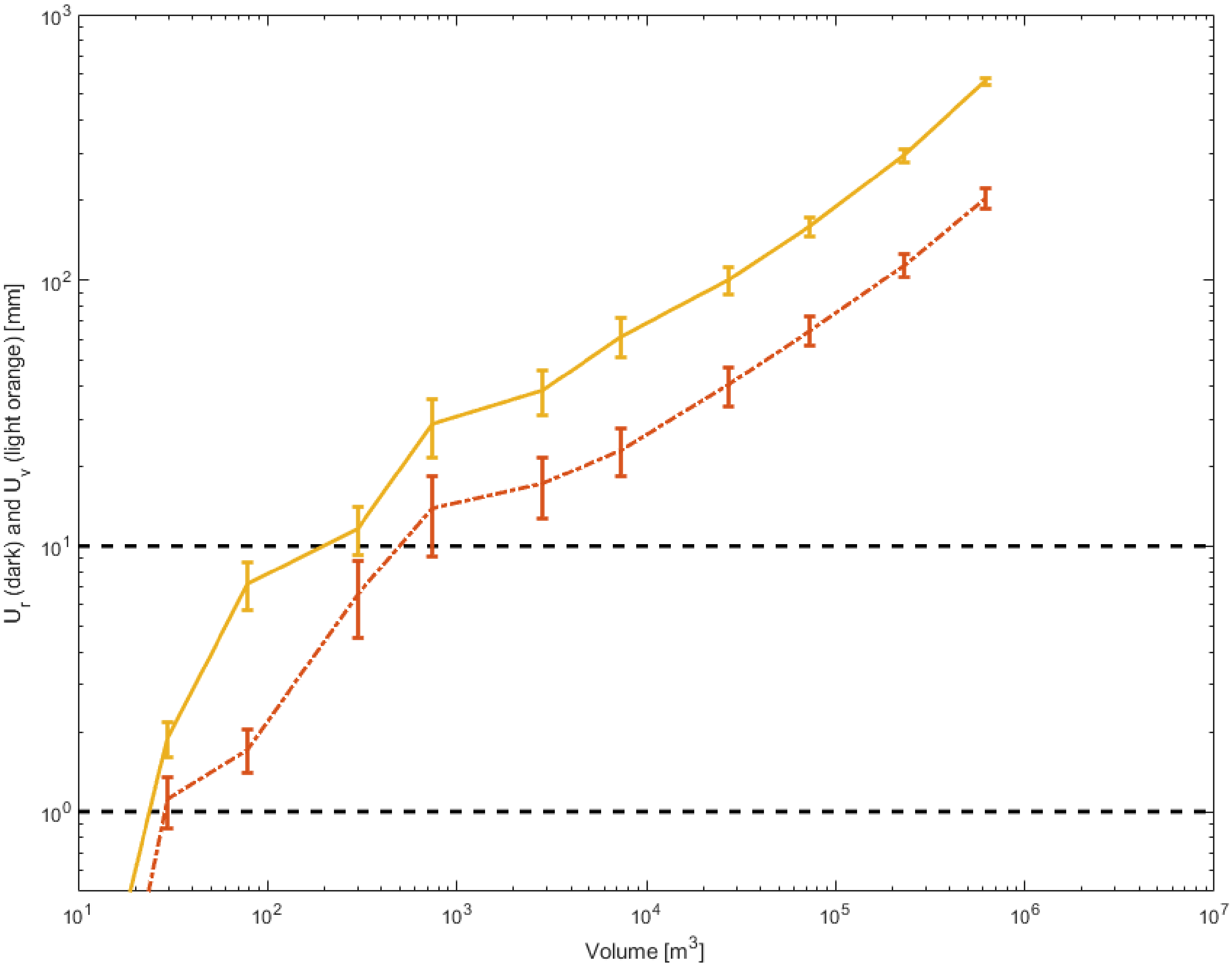

Fig. S15: Geodetic forward modelling tests. *To evaluate whether the seismicity could be related to an additional magmatic intrusion, we simulated displacement fields due to 20000 intrusions injecting in an elastic half-space with variable locations, orientations and sizes-volumes within the depth range of the relocated seismicity (9 to 15 km) to estimate peak horizontal (dark orange) and peak vertical (light orange) displacements due to magmatic injections. Horizontal dashed lines mark displacement values of 1 mm (usual noise level threshold for GNSS detectability) and 1 cm (usual noise level threshold for InSAR detectability). Based on this analysis, we note that only very minor magmatic injections with a volume less than 10^2-10^3 m^3 would be undetected.*

Table S1. *Geodetically constrained quadrangle dike model parameter results using GNSS displacement vectors and ascending and descending InSAR observations (Figs S9 & S10). Summary results of the inversion, reporting inversion search bounds, best-fitting model (blue symbols in Figure S11 and S12), mean (red symbols in Figure S11 and S12) and standard deviations of the model parameters based on the probability density functions, and 95% confidence intervals. Coordinates are in metres in UTM zone 26S.*

Quadrangle dyke model parameters	*Lower param. search bounds*	*Upper param. search bounds*	*Best-fit model param.*	*Mean model param.*	*Std*	*Lower confidence interval (5%)*	*Upper confidence interval (95%)*
Easting (m)	*399000*	*413000*	***405291***	*405829*	*1182*	***403451***	***408459***
Northing (m)	*4275000*	*4282000*	***4279118***	*4279237*	*551*	***4278087***	***4280352***
Top Depth (m)	*-5000*	*500*	***-597***	*-844*	*580*	***-2032***	***292***
Top Length (m)	*1000*	*40000*	***4253***	*4523*	*2558*	***1200***	***10639***
Strike (degrees)	*80*	*150*	***105***	*105*	*7*	***92***	***120***
Dip (degrees)	*50*	*130*	***97***	*96*	*7*	***81***	***108***
Shear angle (deg)	*-40*	*40*	***-11***	*-18*	*11*	***-37***	***5***
Length (m)	*1000*	*45000*	***26683***	*22843*	*7407*	***11666***	***41888***
Bot. Length (m)	*1000*	*40000*	***8094***	*7601*	*4698*	***1393***	***17939***

References

1. Ferreira, A. M. G., Marignier, A., Attanayake, J., Frietsch, M. & Berbellini, A. Crustal structure of the Azores Archipelago from Rayleigh wave ellipticity data. *Geophysical Journal International* **221**, 1232–1247 (2020).
2. Matias, L. *et al.* The 9th of July 1998 Faial Island (Azores, North Atlantic) seismic sequence. *J Seismol* **11**, 275–298 (2007).
3. Cao, A. & Gao, S. S. Temporal variation of seismic b-values beneath northeastern Japan island arc. *Geophysical Research Letters* **29**, 48-1-48–3 (2002).